

Satellite-based Near-Real-Time Global Daily Terrestrial Evapotranspiration Estimates

Lei Huang^{1*}, Yong Luo^{1*}, Jing M. Chen^{2,3}, Qihong Tang^{4,5}, Tammo Steenhuis⁶, Wei Cheng⁷ and Wen Shi¹

¹Department of Earth System Science, Ministry of Education Key Laboratory for Earth System Modeling, Institute for Global Change Studies, Tsinghua University, Beijing 100084, China

²Key Laboratory for Humid Subtropical Ecogeographical Processes of the Ministry of Education, School of Geographical Sciences, Fujian Normal University, Fuzhou, 350007, China

³Department of Geography and Planning, University of Toronto, Ontario, M5S 3G3, ON, Canada

⁴Key Laboratory of Water Cycle and Related Land Surface Processes, Institute of Geographic Sciences and Natural Resources Research, Chinese Academy of Sciences, Beijing 100101, China

⁵University of Chinese Academy of Sciences, Beijing 101408, China

⁶Department of Biological and Environmental Engineering, Cornell University, Ithaca 14850, New York, USA

⁷Key Laboratory of Land Surface Pattern and Simulation, Institute of Geographic Sciences and Natural Resources Research, Chinese Academy of Sciences, Beijing 100101, China

Correspondence to Lei Huang (leihuang007@mail.tsinghua.edu.cn) or Yong Luo (Yongluo@mail.tsinghua.edu.cn)

Abstract.

Accurate and timely ~~information on~~ global ~~terrestrial actual~~ evapotranspiration (ET) ~~data~~ is crucial ~~infor~~ agriculture, water resource management, and drought forecasting ~~in a changing climate~~. ~~While, Although~~ numerous satellite-based ET products ~~have been developed in recent decades, few provide~~ ~~are available,~~ ~~few offer~~ near-real-time ~~global terrestrial ET estimates~~. ~~The MOD16 ET dataset, currently updating at the fastest rate, still experiences a delay of over two weeks. This is because most satellite-based ET algorithms rely on meteorological data from land surface models or in situ measurements, which cannot be obtained in near-real-time, resulting in delays of more than two weeks. To expedite global ET data access, we developed the Moderate Resolution Imaging Spectroradiometer (MODIS) based Variation of~~ ~~. For instance, products like NASA's ECOSTRESS and MOD16 face challenges such as uneven coverage and delays exceeding one week in data availability. In this study, we refined the Variation of the Standard~~ Evapotranspiration Algorithm (VISEA) ~~to provide global daily ET data within a week of the actual measurements at a spatial resolution of 0.05°.~~ The VISEA model incorporates several key components: (1) A vegetation index (VI)-temperature (Ts) triangle method to simulate air temperature (Ta), serves as a basis for calculating other meteorological parameters (e.g., water vapor deficit and wind speed); (2) A daily evaporation fraction (EF) method based on the decoupling parameter, converts satellite-based instantaneous observations into daily ET estimates; (3) A net radiation calculation program takes into account cloud coverage in the atmosphere's downward longwave radiation. The VISEA model is driven by shortwave radiation from ~~theby~~ fully integrating satellite-based data, including European Centre for Medium-range ~~Range~~ Weather Forecasts (ERA5-Land) and MODIS land products, e.g., ~~Land's~~ shortwave radiation, which includes satellite remote sensing data within its assimilation system and MODIS's land surface data ~~include~~ surface reflectance, ~~land surface~~ temperature/emissivity, land cover ~~products,~~ vegetation indices, and albedo as inputs. ~~To assess its~~ It enables VISEA to provide near-real-time global daily ET estimates with a maximum delay of one week at a resolution of 0.05°. Its accuracy, ~~we compared~~

带格式的: 段落间距段后: 1 行

45 VISEA with measurements from was assessed globally using observation data from 149 flux towers,
46 across 12 land cover types and comparing it with five other satellite-based global ET products, and GPCP
47 precipitation data from the Global Precipitation Climatology Centre (GPCC). The evaluations show. The
48 results indicate that the near-real-time ET using VISEA performs with similar VISEA provides
49 comparable accuracy ET estimates to other existing data products and offers a significantly shorter time
50 frame for daily data availability. Over 12 landcover types, the products, achieving a mean correlation
51 coefficient (R-is) of about 0.6 with an RMSE of 1.4 mm day⁻¹ at a daily scale. Furthermore, the
52 consistent spatial pattern of multi-year average VISEA aligns with GPCC precipitation data, showing the
53 ET dataset ability to accurately represent global terrestrial ET distribution. To emphasize the capabilities
54 of the VISEA for we demonstrated VISEA's utility in drought monitoring, we analyzed the spatial and
55 temporal variations of ET during a drought event and subsequent recovery with precipitation in the
56 Yangtze River basin from August 26th to September 2nd, 2022. The VISEA distinctly illustrated low mean
57 ET levels (<0.5 mm day⁻¹) across the Yangtze River Basin on August 28th, indicating in 2022, in which
58 the severity of ET changes correlated with the drought. Conversely, a noticeable increase in ET (>1 mm
59 day⁻¹) is observed on August 30th, signifying the retreat of the drought due to precipitation. The near-real-
60 time global daily terrestrial ET estimates could be a capability of VISEA is, thus, especially valuable for
61 meteorology in meteorological and hydrology/hydrological applications requiring real-time data,
62 particularly in for coordinating drought relief efforts during droughts. The VISEA code and ET dataset
63 are available at <https://doi.org/10.11888/Terre.tpcd.300782> (Huang et al., 2023a).

64 1 Introduction

65 Global terrestrial evapotranspiration (ET) is a vital component of the Earth's water cycle and energy
66 budget. It includes evaporation from the soil and water surfaces (some studies also consider evaporation
67 from the intercepted precipitation in canopies) and plant transpiration (Zhang et al., 2021; He et al., 2022;
68 Wang et al., 2021a). Accurate and timely estimation of ET is essential for quantitatively assessing
69 changes in the water cycle under climate change, vigilant monitoring drought, and effectively managing
70 and allocating water resources (Su et al., 2020; Han et al., 2021; Aschonitis et al., 2022).

71 Near-real-time ET estimation from climate models have Global terrestrial evapotranspiration (ET) is
72 a vital component of the Earth water cycle and energy budget. It includes evaporation from the soil and
73 water surfaces (some studies also consider evaporation from the intercepted precipitation in canopies)
74 and plant transpiration (He et al., 2022; Wang et al., 2021a; Zhang et al., 2021). Accurate and timely
75 estimation of ET is essential for quantitatively assessing changes in the water cycle under climate change,
76 vigilant monitoring drought, and effectively managing and allocating water resources (Aschonitis et al.,
77 2022; Han et al., 2021; Su et al., 2020).

78 Near-real-time ET estimation from reanalysis data has been widely used to assess and predict ET
79 changes in the global water cycle under different weather conditions/climate changes (Copernicus Climate
80 Change Service, 2020). While these models/datasets, such as ERA5 reanalysis (Albergel et al., 2012;
81 Jarlan et al., 2008; Miller et al., 1992) and CRA-40 (Liu et al., 2023; Zhao et al., 2019), offer near-real-
82 time latent heat flux (ET in energy units) with a delay of just six days, but they typically feature coarser

带格式的: 缩进: 首行缩进: 2 字符

设置了格式: 英语(英国)

83 spatial resolutions, often 0.425° or more. This level of resolution may limit their effectiveness for detailed
84 assessments of drought conditions and the optimization of water resource allocation. On the other hand,
85 obtaining highly accurate, near-real-time, or real-time ET measurements through local eddy covariance
86 or lysimeter methods can be very valuable (Awada et al., 2022), but collecting large-scale ET data on a
87 fine grid using this equipment proves to be quite challenging is prohibitively expensive (Barrios et al.,
88 2015; Tang et al., 2009).

89 Satellite remote sensing-based ET estimates outperform climate model simulations by
90 offering reanalysis data by providing high spatial resolution for detailed water use utilization analysis,
91 near-real-time data for prompt environmental response, and global coverage for comprehensive water
92 cycle studies. These ET estimates rely on direct observations, enhancing accuracy, especially where
93 ground data are sparse, and allowing for the dynamic monitoring of land and vegetation changes.
94 This capability underscores their importance in water resource management and climate research,
95 complementing the broader perspectives provided by climate models.

96 The selected ET products discussed in this study embody diverse and innovative algorithmic
97 approaches that below have significantly contributed to estimating global ET estimation and have gained
98 recognition within the scientific community. The MOD16 ET dataset product, developed by Mu et al.
99 (2007, 2011), utilizes a Penman-Monteith-based approach and is driven by MODIS land cover, albedo,
100 fractional photosynthetically active radiation, leaf area index, and daily meteorological reanalysis data
101 from NASA's Global Modelling and Assimilation Office to estimate ET. As the first satellite-based
102 global ET product, it played a pivotal role in providing precise estimations crucial for global drought
103 monitoring (Mu et al., 2013).

104 The AVHRR ET dataset, developed by Zhang et al. (2006, 2009), (GMAO) to estimate ET. The
105 AVHRR ET product, developed by Zhang et al. (2006, 2009), significantly advanced the study of the
106 global water cycle. It employed a modified Penman-Monteith approach over land, integrating biome-
107 specific canopy conductance determined by NDVI, and utilized a Priestley-Taylor approach over water
108 surfaces. These algorithms were driven by AVHRR Global Inventory Modeling and Mapping Studies
109 (GIMMS) NDVI, daily surface meteorology data from the National Centers for
110 Environment Environmental Prediction/National Center for Atmospheric Research (NCEP/NCAR)
111 reanalysis, and solar radiation from NASA/GEWEX Surface Radiation Budget Release-3.0. This dataset
112 has significantly advanced the study of the global water cycle, capitalizing on its extensive coverage and
113 high accuracy to provide valuable insights into global hydrological processes.

114 The FLUXCOM dataset, is notable for its utilization ofThe FLUXCOM framework has made a
115 substantial contribution to resolving the evapotranspiration paradox. It utilizes machine learning to
116 integrate eddy covariance data from the global FLUXNET tower network, surface meteorological data
117 from the Climatic Research Unit (CRU) reanalysis, and remote sensing data. This approach has made a
118 substantial contribution to resolving the evapotranspiration paradox and has cemented its status as a
119 crucial tool widely acknowledged within the scientific community for elucidating intricate ET dynamics.
120 (Jung et al., 2009, 2010, 2019).

设置了格式: 字体: Times New Roman, 10 磅

带格式的: 缩进: 首行缩进: 2 字符

域代码已更改

121 Additionally, GLEAM, developed by Miralles et al. (2011b) and Martens et al. (2017), holds a
122 prominent position as one of the best satellite-based ET products, known for its unparalleled accuracy
123 and using unique algorithmic approaches that have considerably advanced global ET the estimation and
124 enhanced our understanding of land surface evapotranspiration processes. Global ET which uses
125 meteorology data from ECMWF Reanalysis 5. Lastly, PML, developed by Zhang et al. (2019, 2022),
126 represents is the first 250-meter to offer global ET coverage ET product, providing unprecedented spatial
127 at a 500-meter resolution for global ET estimation and contributing, demonstrating high accuracy
128 compared to our understanding of the decline in global water availability local eddy covariance
129 observations worldwide with MODIS satellite data and Global Land Data Assimilation System Version
130 2.1 (GLDAS-2.1) data (Zhang et al., 2023b, 2023).

131 While these satellite-based global ET products provide reasonable estimations, they do not offer
132 near real-time ET estimates. Despite ongoing rapid updates to the MOD16 ET dataset, it still encounters
133 delays exceeding two weeks. Additionally, AVHRR ET spans from 1983 to 2006, PML ET covers the
134 period from 2002 to 2019, FLUXCOM data covers from 1950 to 2016, and GLEAM ET extends from
135 2001 to 2022. Notably, the four later ET products exhibit data gaps exceeding one year, posing challenges
136 for near-real-time estimation. Furthermore, NASA's ECOSystem Spaceborne Thermal Radiometer
137 Experiment on Space Station (ECOSTRESS) aims to deliver global-scale ET estimation (Fisher et al.,
138 2020). However, as of now, the data from ECOSTRESS have not been published, resulting in a lack of
139 satellite-based global near-real-time ET estimation.

140 The Variation of the Moderate Resolution Imaging Spectroradiometer Standard Evapotranspiration
141 Algorithm (VISEA) was introduced by Tang et al. (2009), which was designed for the near-real-time
142 monitoring of crop consumption at the basin scale. Huang et al. (2017) examined its reliability by
143 conducting a comprehensive assessment comparing its ET values with flux tower measurements and
144 other gridded ET datasets across various scales in China. Subsequently, to improve the model, a
145 decoupling parameter for daily evaporation fraction (EF) was introduced (Huang et al., 2021), and the
146 atmospheric emissivity and cloud coverage in the daily net radiation calculation was included (Huang et
147 al., 2023b). Global terrestrial application and evaluation of the developed VISEA algorithm have not
148 been conducted so far. In this study, we employ this VISEA algorithm along with MODIS surface
149 reflectance (MOD09CMG) (Vermote, 2015), land surface temperature/emissivity (MOD11C1) (Wan et
150 al., 2015), land cover products (MCD12C1) (Friedl & Sulla Menashe, 2015), vegetation indices
151 (MOD13C1) (Didan, 2015), albedo (MCD43C3) (Sehaaf & Wang 2015), and hourly shortwave radiation
152 from ECMWF ERA5 Land. However, these ET products cannot provide near-real-time data due to
153 reliance on local ground-based meteorology and land-surface/reanalysis models, which are time-
154 consuming to obtain globally. For example, MOD16 and PML use GMAO and GLDAS-2.1 data,
155 respectively. While AVHRR ET depends on AVHRR satellite data and NCEP/NCAR Reanalysis
156 meteorology data, GLEAM ET uses MODIS satellite data and ECMWF meteorology Reanalysis data.
157 FLUXCOM relies on FLUXNET and the Climatic Research Unit (CRU) reanalysis data, which are not
158 updated in real-time. Recently, NASA's ECOSystem Spaceborne Thermal Radiometer Experiment,
159 mounted on the International Space Station on the Space Station (ECOSTRESS), was designed to

160 [estimate global-scale ET \(Fisher et al., 2019, 2020\). thermal infrared data at 70-meter resolution every 1](#)
161 [to 7 days. This results in uneven global coverage and reduced data frequency, especially in regions like](#)
162 [the Middle East, as noted by Anderson et al., 2021 and Jaafar et al., 2022. In contrast, the VISEA model](#)
163 [uses only MODIS land products and ERA5-Land shortwave radiation, enabling near-real-time ET](#)
164 [estimations.](#)

165 [The objective of this manuscript is twofold: 1\) adapt the VISEA model for near real-time, global](#)
166 [application by replacing land-based solar radiation inputs with hourly shortwave radiation data from](#)
167 [ECMWF ERA5-Land's data assimilation system \(Sabater, 2019\); and 2\) to provide global daily ET](#)
168 [estimates from 2001 to 2022.](#)

169 [The performance globally validate the model using a comprehensive set of VISEA was evaluated](#)
170 [with data from datasets, including meteorological instruments instrument data and eddy covariance](#)
171 [measurements at from 149 FLUXNET flux towers of FLUXNET \(Pastorello et al., 2020\). We assessed](#)
172 [the spatial distribution averages of VISEA by comparing its Additionally, multi-year average with](#)
173 [established ET datasets from GLEAM \(Martens et al., 2017; Miralles et al., 2011\), FLUXCOM \(Jung et](#)
174 [al., 2009, 2010, 2018\), AVHRR \(Zhang et al., 2009, 2010\), MOD16 \(Mu et al., 2007, 2011\), PML \(Zhang](#)
175 [et al., 2019, 2022\)- and precipitation data from the Global Precipitation Climatology Centre \(GPCC\) \(Udo](#)
176 [et al., 2011\)- are also employed in the assessment.](#)

177 2. Methods

178 2.1 Description of the VISEA algorithm

180 VISEA, short for the Variation of the Moderate Resolution Imaging Spectroradiometer Standard
181 Evapotranspiration Algorithm, is a modification of the MODIS standard Evapotranspiration (ET)
182 algorithm. The original MODIS algorithm, created by Mu et al. (2007 and 2011), is based on the Penman-
183 Monteith method. VISEA introduces two significant modifications. First, it employs the Vegetation (VI)-
184 Temperature (Ts) Triangle method, originally developed by Nishida et al. (2003), to estimate air
185 temperature. Second, VISEA incorporates hourly data on shortwave downward radiation from the ERA5-
186 Land dataset to calculate daily average energy. These two advancements enable VISEA to estimate large-
187 scale ET without needing local measurements as supplementary data.

188 Unlike energy budget-based ET algorithms (such as SEBS (Surface Energy Balance System),
189 METRIC (Mapping Evapotranspiration at high Resolution with Internalized Calibration), and
190 Alexi ALEXI (Atmosphere-Land Exchange Inverse), which calculate ET (latent heat flux) as the residual
191 of the net radiation, by subtracting soil heat flux and sensible heat flux. VISEA estimates ET using the
192 Penman-Monteith equation, placing it in a different category of satellite-based global ET products
193 currently in use. VISEA is a two-source model, which means the ~~ET~~ in one grid cell was separated as
194 the transpiration from full vegetation cover and the evaporation from bare soil surface if energy transfer
195 from the vegetation to the soil surface was ignored (Nishida et al., 2003), i.e.,

$$196 \quad ET = f_{veg}ET_{veg} + (1 - f_{veg})ET_{soil} \quad (1)$$

带格式的: 缩进: 首行缩进: 2 字符

设置了格式: 字体颜色: 自动设置

带格式的: 段落间距段前: 0 磅, 段后: 0 磅

带格式的: 缩进: 首行缩进: 2 字符

带格式的: 段落间距段后: 1 行

带格式的: 缩进: 首行缩进: 2 字符, 段落间距段后: 1 行

带格式的: 缩进: 首行缩进: 0 厘米

带格式的: 段落间距段后: 1 行

带格式的: 段落间距段后: 1 行

197 where the subscript "veg" means full vegetation cover and the subscript "soil" indicates the soil exposed
198 to solar radiation (called bare soil); ET_{veg} is the transpiration from full vegetation cover area ($W m^{-2}$),
199 ET_{soil} is the evaporation from bare soil ($W m^{-2}$), f_{veg} is the portion of the area with the vegetation cover,
200 which can be calculated by Normalized Difference Vegetation Index (calculation details are provided in
201 Appendix A, Tang et al., 2009).

202 The available energy Q ($W m^{-2}$), which is the sum of the latent heat flux and sensible heat flux (also
203 known as the net radiation minus soil heat flux) is also separated into the available energy for vegetation
204 transpiration, Q_{veg} ($W m^{-2}$) and Q_{soil} ($W m^{-2}$) for bare soil evaporation, which was expressed by Nishida
205 et al. (2003) as:

$$Q = f_{veg}Q_{veg} + (1 - f_{veg})Q_{soil} \quad (42)$$

207 As satellites like Terra and Aqua only provide instantaneous snapshot observations of the Earth only
208 once a day, a temporal scaling method is needed to convert instantaneous measurements into daily ET
209 values. Nishida et al. (2003) used satellite-based noon time instantaneous evaporation fraction (EF),
210 defined as the ratio of latent heat flux (ET) to available energy as daily EF ($EF = \frac{ET}{Q}$ the calculation of
211 instantaneous EF is described at Appendix B), multiplied the daily Q to calculate daily ET based on
212 the assumption that EF is constant over a day:

$$ET = EF Q \quad (53)$$

214 In the next section, we will detail how VISEA calculates the daily EF , and Q in Equation (5), and
215 also Eq. 3, daily air temperature and Ps,daily land surface temperature.

216 2.1.1 Daily evaporation fraction calculation

217 Combining Eq. 1, 2 and 3, we calculated the instantaneous evaporation fraction, EF^i as:

$$EF^i = f_{veg} \frac{Q_{veg}^i}{Q^i} EF_{veg}^i + (1 - f_{veg}) \frac{Q_{soil}^i}{Q^i} EF_{soil}^i \quad (4)$$

219 EF_{veg}^i and EF_{soil}^i are the instantaneous full vegetation coverage and bare soil EF , respectively. EF_{veg}^i can
220 be expressed as a function of instantaneous parameters (Nishida et al., 2003):

$$EF_{veg}^i = \frac{\alpha \Delta^i}{\Delta^i + \gamma(1 + r_{c,veg}^i / 2r_{a,veg}^i)} \quad (5)$$

222 where α is the Priestley-Taylor parameter, which was set to 1.26 for wet surfaces (De Bruin, 1983); Δ^i is
223 the instantaneous slope of the saturated vapor pressure, which is a function of the temperature ($Pa K^{-1}$);
224 γ is the psychrometric constant ($Pa K^{-1}$); $r_{c,veg}^i$ is the instantaneous surface resistance of the vegetation
225 canopy ($s m^{-1}$); $r_{a,veg}^i$ is the instantaneous aerodynamics resistance of the vegetation canopy ($s m^{-1}$).
226 EF_{soil}^i was expressed by Nishida et al. (2003) as a function of the instantaneous soil temperature and the
227 available energy based on the energy budget of the bare soil:

$$EF_{soil}^i = \frac{T_{soil\ max}^i - T_{soil}^i}{T_{soil\ max}^i - T_a^i} \frac{Q_{soil0}^i}{Q_{soil}^i} \quad (6)$$

where $T_{soil\ max}^i$ is the instantaneous maximum possible temperature at the surface reached when the land surface is dry (K), T_{soil}^i is the instantaneous temperature of the bare soil (K), T_a^i is the instantaneous air temperature, Q_{soil0}^i is the instantaneous available energy for bare soil when T_{soil}^i is equal to T_a^i ($W\ m^{-2}$).

As the assumption of EF^i = noon time instantaneous evaporation fraction EF^i equals daily average evaporation fraction EF^d , thus, $EF^i = EF^d$, caused a 10%-30% underestimation of daily ET (Huang et al., 2017; Yang et al., 2013), we introduced a decoupling parameter to convert EF^i into EF^d following the algorithm of Tang et al. (2017a, 2017b). This new decoupling parameter-based evaporation fraction is developed from Penman-Monteith and McNaughton-Jarvis mathematical equations:

$$EF^d = EF^i \frac{\Delta^d}{\Delta^{d+\gamma}} \frac{\Delta^{d+\gamma}}{\Delta^i} \frac{\Omega^{*i}}{\Omega^{*d}} \quad (6)$$

where superscript "d" means daily; the EF^i is the instantaneous evaporation fraction; Ω , we introduced a decoupling parameter to convert EF^i into EF^d (Huang et al., 2021; Tang et al., 2017; Tang and Li, 2017). The superscript "d" means daily and "i" means instantaneous. This new decoupling parameter-based evaporation fraction is developed from Penman-Monteith and McNaughton-Jarvis mathematical equations:

$$EF^d = EF^i \frac{\Delta^d}{\Delta^{d+\gamma}} \frac{\Delta^{d+\gamma}}{\Delta^i} \frac{\Omega^{*i}}{\Omega^{*d}} \quad (7)$$

where Ω is the decoupling factor that represents the relative contribution of radiative and aerodynamic terms to the overall evapotranspiration (Tang and Li, 2017), Ω_i^* is the value of the decoupling factor, Ω for wet surfaces. According to Pereira (2004), Ω and Ω^* (the calculation details of Ω and Ω^* are presented in Appendix C-B).

For full vegetation-covered areas, the decoupling parameter based daily EF_{veg}^d is expressed as:

$$EF_{veg}^d = \frac{\alpha \Delta^i}{\Delta^{d+\gamma} \left(1 + \frac{r_{c\ veg}^i}{2r_{a\ veg}}\right)} \left(\frac{\Delta^d}{\Delta^{d+\gamma}} \frac{\Delta^{d+\gamma}}{\Delta^i} \frac{\Omega_{veg}^{*i}}{\Omega_{veg}^{*d}} \frac{\Omega_{veg}^d}{\Omega_{veg}^i} \right) \quad (78)$$

where $r_{c\ veg}^i$ is the instantaneous canopy resistance ($s\ m^{-1}$), $r_{a\ veg}^i$ is the instantaneous aerodynamic resistance ($s\ m^{-1}$). Determining these resistances are presented in Appendix D.

C. For bare soil, the decoupling parameter based daily EF_{soil}^d is calculated as:

$$EF_{soil}^d = \frac{T_{soil\ max}^i - T_{soil}^i}{T_{soil\ max}^i - T_a^i} \frac{Q_{soil0}^i}{Q_{soil}^i} \left(\frac{\Delta^d}{\Delta^{d+\gamma}} \frac{\Delta^{d+\gamma}}{\Delta^i} \frac{\Omega_{soil}^{*i}}{\Omega_{soil}^{*d}} \frac{\Omega_{soil}^d}{\Omega_{soil}^i} \right) \quad (89)$$

Thus, EF^d is expressed as:

$$EF^d = f_{veg} \frac{Q_{veg}^i}{Q^i} EF_{veg}^d + (1 - f_{veg}) \frac{Q_{soil}^i}{Q^i} EF_{soil}^d \quad (9) \quad (10)$$

带格式的: 段落间距段后: 1行

设置了格式: 字体: Cambria Math

带格式的: 缩进: 首行缩进: 2字符

带格式的: 缩进: 首行缩进: 0厘米

带格式的: 缩进: 首行缩进: 0厘米

256 [The same energy balance equations are used for calculating both instantaneous values \$Q^i\$, \$Q_{veg}^i\$ and \$Q_{soil}^i\$](#)
 257 [and daily values \$Q^d\$, \$Q_{veg}^d\$ and \$Q_{soil}^d\$ but with parameters adjusted for each timeframe. The details of the](#)
 258 [calculation for the daily values are outlined below.](#)

259 2.1.2 Daily calculation of available energy Q_{veg}^d and Q_{soil}^d

260 We used an improved daily available energy Q ($W m^{-2}$) method (Huang et al., 2023) for the
 261 vegetation and the bare soil surface is calculated by the energy balance equation:

$$262 R_n - G = Q \quad (4011)$$

263 where R_n is the net radiation ($W m^{-2}$), which could be calculated by the land surface energy balance; G
 264 is the soil heat flux ($W m^{-2}$), $G \approx 0$ on a daily basis (Fritschen and Gay, 1979; Nishida et al., 2003; Tang et
 265 al., 2009),

$$266 R_n^d = (1 - albedo^d)R_a^d - \varepsilon_s^d \sigma T_s^{d4} + (1 + Cloud^d)\varepsilon_a^d \sigma T_a^{d4} \quad (4112)$$

267 [Where \$albedo^d\$ is the daily albedo of the soil surface; \$R_a^d\$ is daily incoming shortwave radiation](#)
 268 [\(\$W m^{-2}\$ \), obtained from the ERA5_Land shortwave radiation \(we called ERA5_Rd\); \$\varepsilon_s^d\$ and \$\varepsilon_a^d\$ are the](#)
 269 [daily emissivity of land surface and atmosphere; \$\sigma\$ is the Stefan-Boltzmann constant;](#)
 270 [\$T_a^d\$ is the daily near-surface air temperature \(K\); \$T_s^d\$ is the daily surface temperature \(K\). The difference](#)
 271 [with the former study provided by Huang et al., \(2021\), which set we is that \$\varepsilon_s^d\$ and \$\varepsilon_a^d\$ were not set](#)
 272 [equal. Instead we calculated the \$\varepsilon_a^d\$ by Appendix E following studying the method of Brutsaert, \(1975\)](#)
 273 [and Wang and Dickinson\(2013\), as detailed in Appendix D and \$\varepsilon_s^d\$ can be retrieved by was retrieved from](#)
 274 [MOD11C1; \$\sigma\$ is the Stefan Boltzmann constant; \$T_a^d\$ is the daily near surface air temperature \(K\); \$T_s^d\$ is](#)
 275 [the daily surface temperature \(K\).](#)

276 We account for the influence of clouds by assuming a linear correlation between downward
 277 longwave radiation and cloud coverage in the calculation of ~~downwards~~downward longwave radiation
 278 based on the study of Huang et al., (2023):

$$279 Cloud = (Cloud^d = (1 - K_t) \quad (4213)$$

280 where $Cloud^d$ is the daily clearness index and K_t is (Chang and Zhang, 2019; Goforth et al., 2002)

$$281 K_t = \frac{R_g^d}{R_a^d} \quad (4314)$$

282 $Cloud^d$ is derived from the clearness index K_t (Chang and Zhang, 2019; Goforth et al., 2002). R_g^d is the
 283 daily extraterrestrial radiation calculated by the FAO (1998).

284 According to Huang et al. (2023), Q_{veg}^d can be calculated by assuming as $T_s^d = T_a^d$ according to the
 285 VI-Ts method which implies that the minimum land surface temperature occurs in fully vegetated grid
 286 cells and is equivalent to T_a^d .

带格式的: 缩进: 首行缩进: 2 字符

设置了格式: 英语(英国)

带格式的: 缩进: 首行缩进: 2 字符

287 where R_a^d is the daily extraterrestrial radiation calculated by the FAO (1998).

288 Q_{veg}^d can be calculated by assuming as $T_s^d = T_a^d$ according to the VI-Ts method which implies that
289 the minimum land surface temperature occurs in fully vegetated grid cells and is equivalent to T_a^d (Huang
290 et al., 2023). According to the land surface energy budget, the daily available energy of vegetation
291 coverage area, Q_{veg}^d and bare soil Q_{soil}^d can be calculated following the study of Huang et al. (2023):

$$292 \quad Q_{veg}^d = (1 - albedo^d)R_a^d + (1 + Cloud^d)\epsilon_a^d \sigma T_a^{d4} - \epsilon_s^d \sigma T_s^{d4} \quad (4415)$$

$$293 \quad Q_{soil}^d = (1 - C_G)(1 - albedo^d)R_a^d + (1 + Cloud^d)\epsilon_a^d \sigma T_a^{d4} - \epsilon_s^d \sigma T_s^{d4} \quad (4516)$$

294 The daily mean air temperature, T_a^d can be extended by a sin and cos function based on the
295 instantaneous air temperature T_a^i which was calculated using the linear correlation between vegetation
296 index (VI) and surface temperature (Ts) method. Thus, $(1 + Cloud^d)\epsilon_a^d \sigma T_a^{d4}$ is the daily downward
297 longwave radiation ($W m^{-2}$), and $\epsilon_s^d \sigma T_s^{d4}$ is the daily upward longwave radiation ($W m^{-2}$), where C_G is
298 an empirical coefficient ranging from 0.3 for a wet soil to 0.5 for a dry soil (Idso et al., 1975).

299 Q_{veg}^d and Q_{soil}^d are calculated by the energy balance equations, which are robust on both
300 instantaneous and daily scales. Thus instantaneous Q_{veg}^i and Q_{soil}^i are calculated by the same set of
301 equising Eq 17 and 18 by replacing the daily by the instantaneous parameters.

302 Following the study of Huang et al. (2023), the daily ET^d can be calculated by the daily EF^d and
303 Q^d as:

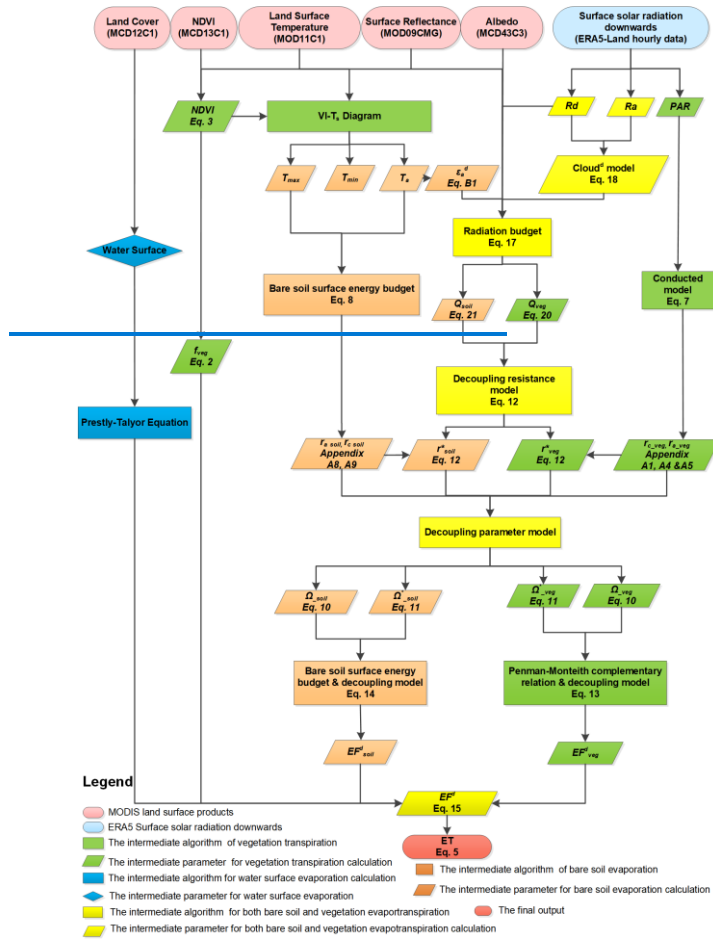
$$304 \quad ET^d = EF^d Q^d \quad (4617)$$

305 Figure 1 illustrates the workflow of VISEA.
306

设置了格式: 英语(美国)

带格式的: 缩进: 首行缩进: 2 字符

带格式的: 缩进: 首行缩进: 2 字符, 无孤行控制



307

308

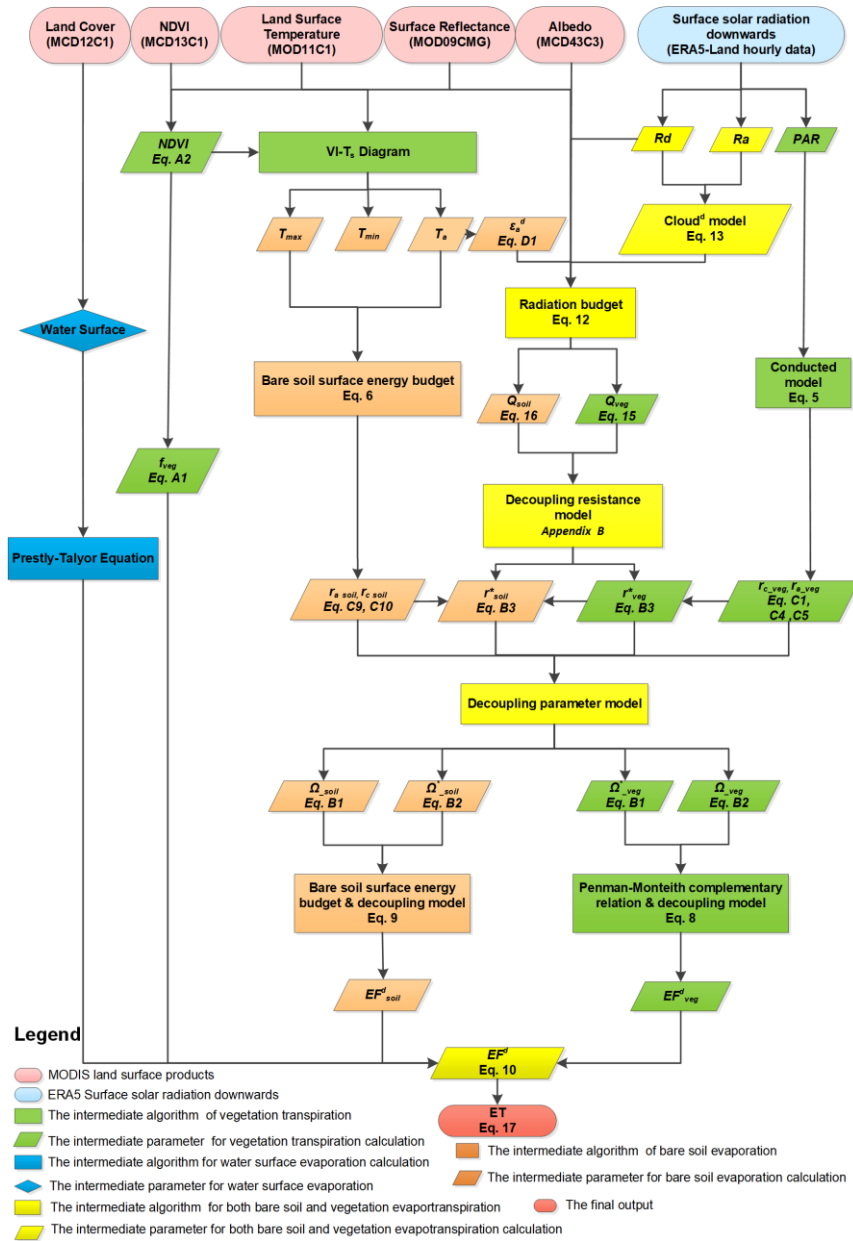
309

310

311

312

Figure 1 illustrates the workflow of VISEA. VISEA utilizes land cover data from the MOD12C1 IGBP land cover classification. When land cover in a MOD12C1 IGBP data grid cell is identified as a water surface, VISEA then uses the Priestley-Taylor equation to compute water surface evaporation. This process guarantees that the unique attributes of water surfaces are precisely reflected in VISEA ET calculations.



313

314 **Figure 1.** Schematic of VISEA algorithm. The ovals in the top row are the databases, and the square
 315 boxes are the algorithms, and parallelograms are the parameters. The numbers in the parenthesis are the
 316 equation to determine the parameters.

317

带格式的: 段落间距段后: 1 行

318 **2.1.3 The calculation of daily air temperature, T_a^d and surface temperature, T_s^d**

319 Daily air temperature, T_a^d is a critical parameter in the VISEA algorithm, used in calculations for
320 downward longwave radiation, daily aerodynamic resistance, and surface resistance. The key innovation
321 in calculating T_a^d , involves employing the VI-Ts method to estimate instantaneous air temperature, T_a^i
322 during the daytime.

323 **This 2.1.3 The calculation of daily air temperature, T_a^d and surface temperature, T_s^d**

324 Daily air temperature, T_a^d is a critical parameter in the VISEA algorithm, used in calculations for
325 downward longwave radiation, daily aerodynamic resistance, and surface resistance. The key innovation
326 in calculating T_a^d , involves employing the VI-Ts method to estimate instantaneous air temperature, T_a^i
327 during the daytime (Huang et al., 2017; Nishida et al., 2003; Tang et al., 2009).

328 This VI-Ts method was developed based on the empirical linear relationship between the surface
329 temperature (Ts) and the Vegetation Index (VI). Surface temperature increases when the vegetation index
330 decreases, and conversely, surface temperature decreases when the vegetation index increases. By
331 defining a "window" formed in the scatter plot, defined by VI (horizontal axis) and Ts (vertical axis) from
332 the neighboring 5 * 5 grid cells, the scatter plot of these 25 grid cells' VI and Ts typically exhibits a
333 triangular (or trapezoidal) distribution. In this scatter plot, we identify the "warm edge" (characterized by
334 a low vegetation cover fraction and high Ts) and the "cold edge" (marked by a high vegetation cover
335 fraction and low Ts).

336 The warm edge is automatically selected as the hypotenuse of the triangle formed by these scatter
337 points. Through simple interpolation, Ts corresponding to any given vegetation condition within the
338 range of the "warm edge" and "cold edge" can be determined. The lowest Ts could be determined by the
339 highest VI, and the highest Ts could be determined by the lowest VI. Therefore, following Nishida et al.
340 (2003), under the assumption assuming that the lowest surface temperature equals the air temperature (Ta),
341 we can derive the daily air temperature.

342 For nighttime periods, it is assumed that air temperature is equivalent to the nighttime land surface
343 temperature provided by MOD11C1. These two temperature estimates are then extended into hourly air
344 temperature profiles using a sine-cosine fitting curve. The 24-hour average of T_a^i is used as T_a^d . Similarly,
345 T_s^d is calculated using MOD11C1 land surface temperature data for both daytime and nighttime. These
346 estimates are extended into hourly surface temperature profiles using a similar sine-cosine fitting curve,
347 and the daily average of T_s^d is determined (Huang et al., 2021).

348 A key advance of this VISEA algorithm is the application of the VI-Ts method to calculate $T_{soil-max}^i$
349 and T_a^i (Huang et al., 2017; Nishida et al., 2003; Tang et al., 2009). The VI-Ts method is based on the
350 empirical linear relationship between the vegetation index (VI), typically calculated by NDVI, and land
351 surface temperature (Ts). When plotted on a two-dimensional scatter plot, VI and Ts generally form a
352 trapezoid or triangular shape. In these plots, regions with low VI and high Ts values constitute the "warm
353 edge," while areas with high VI and low Ts values form the "cold edge." Using simple linear interpolation,

带格式的: 缩进: 首行缩进: 0.35 厘米

354 Ts values corresponding to any given VI between the "warm edge" and the "cold edge" can be determined.
 355 Assuming $T_s = T_a^i$ for cases where the highest VI corresponds to the lowest Ts, we can calculate T_a^i .
 356 Similarly, $T_{soil,max}^i$ can be easily calculated since it corresponds to the lowest VI.

357 This VI-Ts method allows for the estimation of T_a^i and $T_{soil,max}^i$ without the need for additional
 358 meteorological data. However, some studies have found that the VI-Ts method may not consistently
 359 provide satisfactory results, especially in colder regions where vegetation thrives better under higher
 360 temperatures.

361 2.2 Technical validation

362 The correlation coefficient, Root Mean Square Error (RMSE) and Nash-Sutcliffe efficiency
 363 coefficient are used to evaluate our global daily ET estimates with eddy covariance measurements and
 364 compared with the other five independent global ET products on a monthly scale.

365 The correlation coefficient R is calculated as:

$$366 R = \frac{\sum(X-\bar{X})(Y-\bar{Y})}{\sqrt{\sum(X-\bar{X})^2\sum(Y-\bar{Y})^2}} \quad (4718)$$

367 R is the correlation coefficient; X is the estimated variable; \bar{X} is the average of X; Y is the observed
 368 variable; \bar{Y} is the average of Y.

369 The Root Mean Square Error (RMSE) is calculated as:

$$370 RMSE = \sqrt{\frac{\sum_{i=1}^N (X_i - Y_i)^2}{N}} \quad (4819)$$

371 For a more nuanced understanding of the Root Mean Square Error (RMSE), we have deconstructed
 372 it into two distinct components: RMSEs (systematic RMSE) and RMSEu (unsystematic RMSE). This
 373 breakdown allows a more detailed examination of the systematic and unsystematic sources contributing
 374 to the overall error metric.

375 The systematic Root Mean Square Error (RMSEs) is calculated as:

$$376 RMSEs = \sqrt{\frac{\sum_{i=1}^N (Z_i - Y_i)^2}{N}} \quad (4920)$$

377 The unsystematic Root Mean Square Error (RMSEu) is calculated as:

$$378 RMSEu = \sqrt{\frac{\sum_{i=1}^N (Z_i - X_i)^2}{N}} \quad (2021)$$

379 Where $Z_i = a + bY_i$, where a and b are the least squares regression coefficients of the estimated variable
 380 X_i and observed variable Y_i , N is the sample size (Norman et al., 1995).

381 The Nash-Sutcliffe efficiency coefficient (NSE)

带格式的: 缩进: 首行缩进: 2 字符

设置了格式: 英语(英国)

382
$$NSE = 1 - \frac{\sum(X_i - Y_i)^2}{\sum(Y_i - \bar{Y})^2} \quad (2122)$$

383 The ratio of the standard deviations of X and Y

384
$$Ratio = \frac{X_{Standard\ Deviation}}{Y_{Standard\ Deviation}} \quad (2223)$$

385 The Bias of X and Y

386
$$Bias = \bar{X} - \bar{Y} \quad (2324)$$

387 **2.3 The gap-filling of MODIS data**

388 MODIS sensors on board of Terra and Aqua observe the Earth twice a day. However, there are
 389 always data gaps in the MODIS land products because of cloud cover problems. In the VISEA algorithm,
 390 we used the neighboring days' available data to fill the data gaps. According to the study of Tang et al.
 391 (2009), the cloud gaps don't reduce the accuracy of this algorithm significantly.

392 **2.3 The gap-filling of MODIS data**

393 MODIS sensors on board of Terra and Aqua observe the Earth twice a day. However, there are
 394 always data gaps in the MODIS land products because of cloud cover problems. In the VISEA algorithm,
 395 we used the data from the neighboring days to fill the data gaps. The periods when MODIS Land
 396 temperature data were missing, primarily due to cloud cover, accounted for approximately one-third of
 397 the observation period. The accuracy of this gap-filling method is evaluated in Section 4.

398 **3. Data**

399 **3.1 The input data**

400 The input data including the MODIS land products: daily 0.05° surface reflectance (MOD09CMG),
 401 land surface temperature/emissivity (MOD11C1) and albedo (MCD43C3), 8-day 0.05° vegetation
 402 indices (MOD13C1) and yearly 0.05° land cover products (MCD12C1). We also used hourly downward
 403 surface solar radiation from the Fifth Generation of the European Centre for Medium-Range Weather
 404 Forecasts (ECMWF) Reanalysis (ERA5), “ERA5-Land hourly data from 1950 to present” data as energy
 405 input of VISEA algorithm. The surface solar radiation data from ERA5-Land and land data products from
 406 MODIS land products are both near-real-time datasets with a one-week delay, enabling VISEA to provide
 407 global near-real-time ET estimations. Details of the input data, their download links, variable names, used
 408 parameters, spatial and temporal resolution are given in Table 1.

409 **Table 1. The input of VISEA**

The input of VISEA			
Data source	Data name	Used parameter	Spatial/temporal resolution
MODIS Land	MOD11C1	Land Surface Temperature	0.05°/ daily

Product	MOD09CMG	Surface Reflectance	0.05°/daily
	MCD43C3	Albedo	0.05°/daily
	MOD13C1	NDVI	0.05°/16-day
	MCD12C1	Land cover/Cover	0.05°/ yearly
ERA5-Land hourly data	Rd	Downward surface solar radiation/Surface Solar Radiation	0.1°/ hourly

设置了格式: 字体: Times New Roman, 10 磅, 加粗, 英语(英)

带格式的: 无孤行控制

设置了格式: 字体: (默认) Arial Unicode MS, 12 磅, 非加粗, 英语(美国)

带格式的: 段落间距段前: 1 行, 段后: 0 磅

带格式的: 段落间距段前: 0 磅, 行距: 1.5 倍行距

410

3.2 The evaluation data

3.2.1 The flux tower measurements from FLUXNET

We evaluated the accuracy of the input ERA5-Land shortwave radiation, estimated daily net radiation, air temperature, and ET by comparing them against measurements from FLUXNET2015 (Pastorello et al., 2020). ~~The data from FLUXNET2015 can be obtained at <https://fluxnet.org/data/download-data>. While there are records from a total of 212 flux towers in our datasets, not all of them met our stringent inclusion criteria. Each site needed to fulfill~~ FLUXNET consists of 212 globally distributed flux towers and it has implemented quality control measures for energy closure and is considered reliable (Baldocchi et al., 2001; Pastorello et al., 2020; Wang et al., 2022). ~~The data from FLUXNET2015 can be obtained at <https://fluxnet.org/data/download-data>. We selected data from 2001 to 2015 and excluded sites with zero ERA5-Land downward shortwave radiation.~~

~~While there are records from 212 flux towers in our datasets, not all met the stringent inclusion criteria. Each site needed to fulfill~~ three specific requirements to be included in our analysis: (1) availability of data for the period spanning from 2001 to 2015; (2) ERA5-Land downward shortwave radiation greater than 0 within the $0.1^\circ \times 0.1^\circ$ grid cell corresponding to the flux tower's location; (3) conformity with MODIS land cover data (MOD12C1) at the $0.05^\circ \times 0.05^\circ$ grid cell level, ensuring that the flux tower was situated on land rather than over the ocean. ~~In our evaluation using FLUXNET observational data, we leveraged FLUXNET's diligent efforts in addressing energy closure concerns. Specifically, FLUXNET has implemented rigorous measures for energy closure corrections and validations, thereby enhancing the reliability of the observational data from the 212 globally distributed flux towers (Pastorello et al., 2020; Baldocchi et al., 2001; Wang et al., 2022). We selected data spanning the period from 2001 to 2015 and excluded sites where ERA5 Land downward shortwave radiation was zero.~~

设置了格式: 字体: Times New Roman, 10 磅

~~Our study incorporates data from a carefully selected~~ Based on these criteria, we selected a subset of 149 flux towers that met these stringent criteria. This approach ensures the reliability and relevance of our analysis. The distribution of these 149 flux towers is presented in Figure 2. Supplementary Table S1 shows the longitude, latitude, elevation, and land cover type (classified by the International Geosphere-Biosphere Programme, IGBP) of these sites. The 149 sites covered 12 IGBP land cover types: 18 croplands (CRO), 1 closed shrublands (CSH), 15 deciduous broadleaf forests (DBF), 1 deciduous needle leaf forest (DNF), 10 evergreen broadleaf forests (EBF), 34 evergreen needle leaf forests (ENF), 30 grasslands (GRA), 5 mixed forests (MF), 8 open shrublands (OSH), 8 savannas (SAV), 13 wetlands (WET), and 6 woody savannas (WSA).

带格式的: 孤行控制

442 **3.2.2 The other gridded ET and precipitation products**

443 We also used five independent globally gridded ET products and one precipitation product
 444 for product were used to evaluate VISEA estimated ET's comparison. The five ET products include
 445 two MODIS-based ET products: MOD16 (Mu et al., 2007, 2011) and Penman-Monteith-Leuning
 446 Evapotranspiration V2 (PML) (Zhang et al., 2019, 2022), one AVHRR-based AVHRR ET (Zhang et al.,
 447 2009, 2010), one machine learning algorithm output, the FLUXCOM ET data (Jung et al., 2009, 2010,
 448 2018, 2019) and one multiple-satellites data based Global Land Evaporation Amsterdam Model (GLEAM)
 449 ET (Martens et al., 2017; Miralles et al., 2011). The precipitation data was from the Global Precipitation
 450 Climatology Centre (GPCC), which is based on local measurements (Schneider et al., 2014, 2017; Becker
 451 et al., 2013)(Becker et al., 2013; Schneider et al., 2014, 2017) and Global Unified Gauge-Based Analysis
 452 of Daily Precipitation (GPC). Details of these five ET products and the precipitation data are given in
 453 Table 2. To maintain the consistency in temporal and spatial resolution for comparison purposes, we
 454 obtained monthly MOD16 and PML, despite their original temporal resolution of 8 days and We used
 455 the 0.05°×0.05° version of MOD16, AVHRR ET and PML. Additionally, for multi-year scale
 456 comparisons, we confined our dataset to the timeframe between 2001 and 2020. This selection enabled
 457 us to utilize a diverse range of ET products, effectively minimizing the influence of temporal
 458 discrepancies on our comparative analysis. We also incorporated daily Evapotranspiration (ET) data from
 459 GLEAM and VISEA, alongside precipitation data from the Climate Prediction Center (CPC), spanning
 460 from July 25th to August 2nd, 2022. This allowed for near-real-time analysis of ET and precipitation
 461 during the Yangtze River drought incident within that interval, despite the datasets potentially
 462 encompassing more extensive periods.

带格式的: 缩进: 首行缩进: 2 字符

463 **Table 2.** The five global girded ET products and one precipitation product used for comparison with our
 464 near-real-time global daily terrestrial ET estimates.

带格式的: 段落间距段后: 0 磅, 孤行控制

Product name	Spatial/Temporal resolution	Time period	Theory
GLEAM	0.25°/Monthly	2001-2022	Priestly-Taylor Equation
FLUXCOM	0.5°/Monthly	2001-2016	Machine learning Learning
MOD16	0.05°/Monthly	2001-2014	Penman-Monteith Equation
AVHRR	1°/Monthly	2001-2006	Improved Penman-Monteith Equation
PML	0.05°/8-day	2003-2018	Penman-Monteith Equation and a diagnostic biophysical model A Diagnostic Biophysical Model
GPCC	0.25°/Monthly	2001-2019	In-situ observations Observations
GPC	0.5°/Daily	08/28/2022-09/01/2022	Global Unified Gauge-Based Analysis of Daily Precipitation

带格式的: 行距: 单倍行距

格式化表格

带格式的: 行距: 单倍行距

带格式的: 行距: 单倍行距

带格式的: 行距: 单倍行距

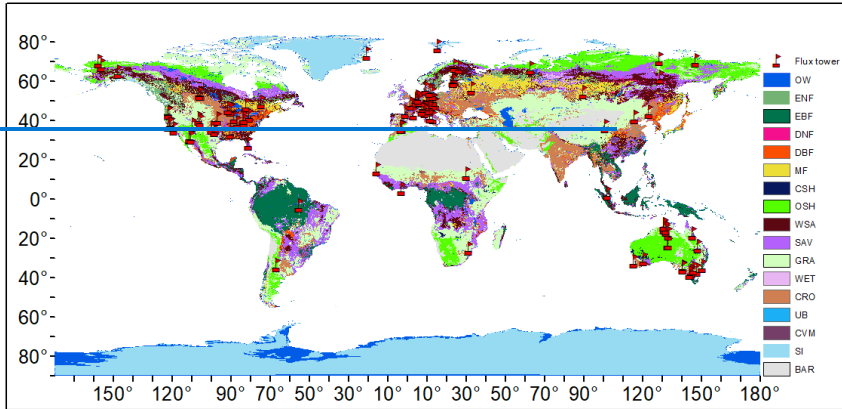
带格式的: 行距: 单倍行距

带格式的: 行距: 单倍行距

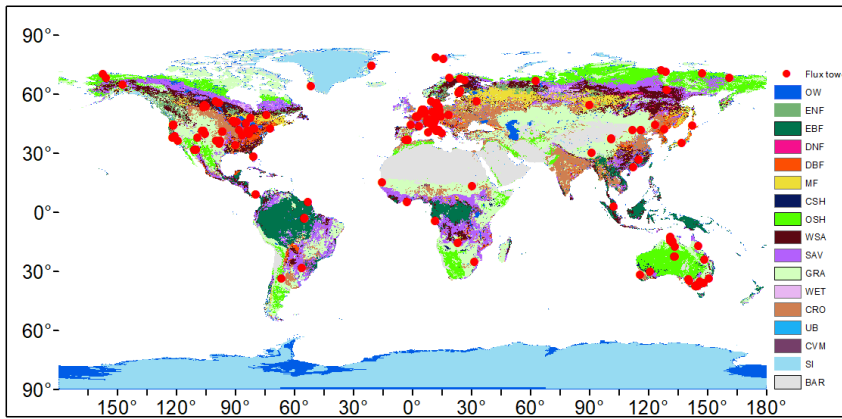
带格式的: 行距: 单倍行距

带格式的: 行距: 单倍行距

465 设置了格式: 字体: Times New Roman, 10 磅



466
467



468

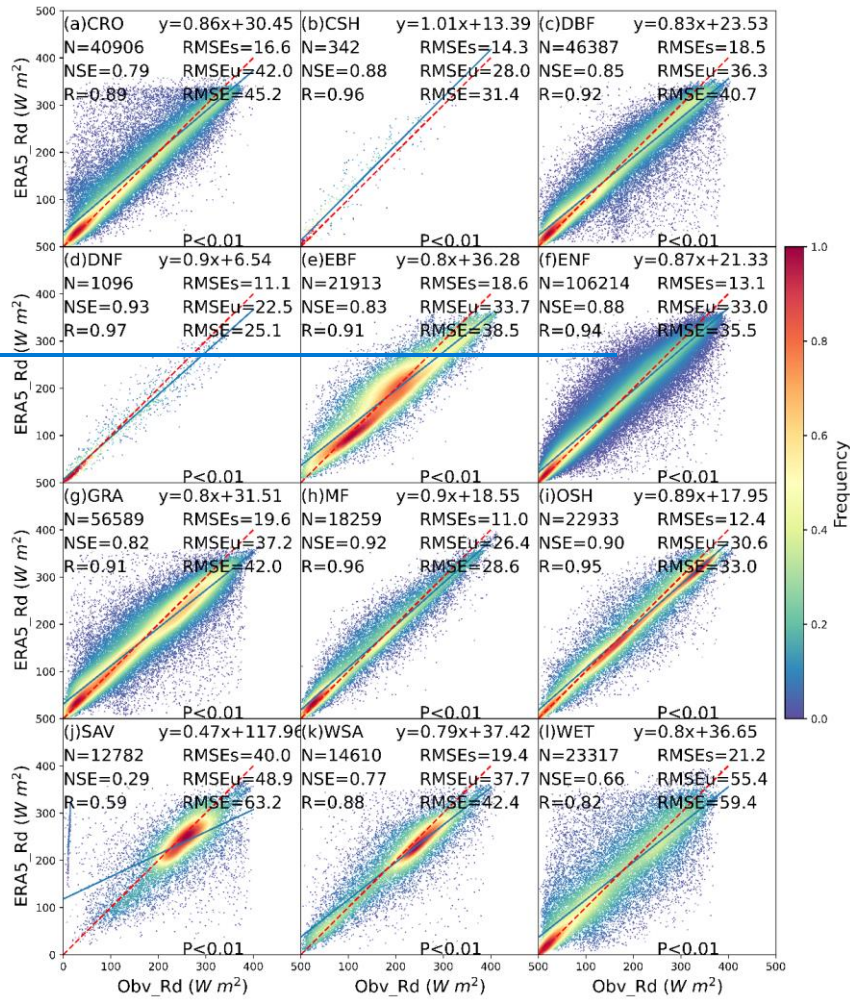
469 **Figure 2.** The distribution of 149 flux towers from FLUXNET in different IGBP land cover types,
 470 specifically OW (Water bodies), ENF (Evergreen needle leaf forests), EBF (Evergreen broadleaf forests),
 471 DNF (Deciduous needle leaf forests), DBF (Deciduous broadleaf forests), MF (Mixed forests), CSH
 472 (Closed shrublands), OSH (Open shrublands), WSA (Woody savannas), SAV (Savannas), GRA
 473 (Grasslands), WET (Permanent wetlands), CRO (Croplands), UB (Urban and built-up lands), CVM
 474 (Cropland/natural vegetation mosaics), SI (Snow and ice), BAR (Barren).

475 **4. Results**

476 [In our initial analysis](#) To evaluate the performance of ERA5_Rd across different land cover initial
 477 [categories](#), we juxtaposed downward solar radiation input data from ERA5-Land (ERA5_Rd) with
 478 measurements obtained from 149 flux towers (Obv_Rd) across diverse IGBP land cover types, as
 479 illustrated in Figure 3. The results indicate a commendable agreement between ERA5_Rd and Obv_Rd
 480 measurements for the majority of land covers, with notable exceptions observed in savanna (SAV).
 481 Specifically, the mean Nash-Sutcliffe Efficiency (NSE) stands at 0.84, the mean correlation coefficient
 482 (R) at 0.92, and the mean Root Mean Square Error (RMSE) at 38.3 W m⁻². [This comparative analysis](#)
 483 [offers helpful insights into the performance of ERA5_Rd across different land cover categories.](#)

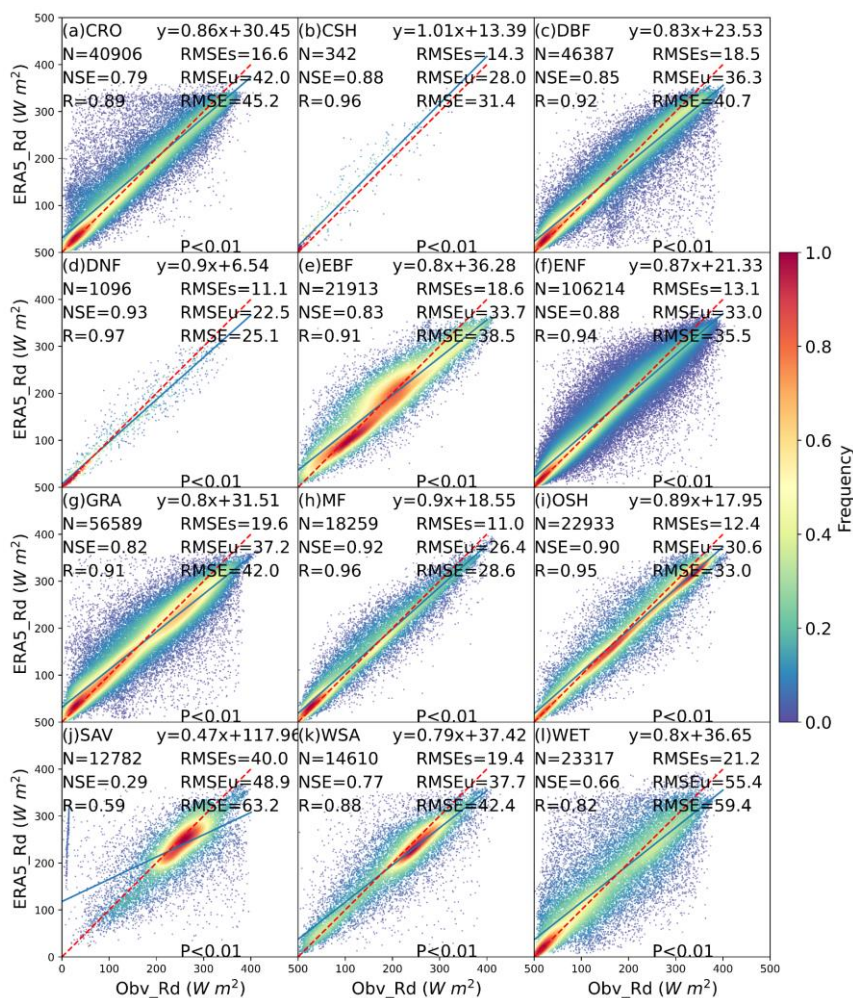
带格式的: 段落间距段后: 1 行

带格式的: 段落间距段前: 0 磅, 段后: 0 磅, 行距: 1.5 倍行距



485 [Figure 3 shows that ERA5 input shortwave radiation generally agrees well with local measurements.](#)
 486 [ERA5_Rd exhibits optimal performance in DNF and MF, reflected by NSE and R values surpassing 0.9.](#)
 487 [In these land covers, the mean RMSEs stand at 11 W m⁻², mean RMSEu at 24.5 W m⁻², and mean RMSE](#)
 488 [at 26.9 W m⁻². However, its performance in SAV is notably subpar, characterized by an NSE of 0.29, an](#)
 489 [R of 0.59, highest RMSEs of 40 W m⁻², RMSEu of 48.9 W m⁻², and RMSE of 63.2 W m⁻². For ERA5_Rd,](#)
 490 [the mean RMSEs amount to 16 W m⁻², and the mean RMSEu is 34.8 W m⁻², suggesting that ERA5_Rd](#)
 491 [demonstrates high accuracy by effectively capturing the systematic variation in Obv_Rd, as indicated by](#)
 492 [its relatively low RMSEs and RMSEu close to RMSE \(Willmott et al., 1981\) in most land covers, except](#)
 493 [for SAV. Specifically, in Figure 3, Rd s derived from ERA5 exhibit very low P-values \(<0.01\).](#)

494



495

496 **Figure 3.** The scatter plot of downward solar radiation from ERA5-Land (ERA5_Rd) compared with

497 local instruments measurements (Obv_Rd) under 12 IGBP land cover types: CRO (Croplands), CSH
498 (Closed shrublands), DBF (Deciduous broadleaf forests), DNF (Deciduous needle leaf forests), EBF
499 (Evergreen broadleaf forests), ENF (Evergreen needle leaf forests), GRA (Grasslands), MF (Mixed
500 forests), OSH (Open shrublands), SAV (Savannas), WSA (Woody savannas), WET (Permanent
501 wetlands). The red dotted line is the 1:1 line. N is the number of data points, NSE is Nash-Sutcliffe
502 Efficiency, R is correlation coefficients, RMSE is Root Mean Square Error, RMSEs is systematic RMSE,
503 and RMSEu is unsystematic RMSE. The Frequency denotes the probability density estimated through
504 the KDE method with a Gaussian kernel, and it is then scaled to ensure that the maximum value of the
505 probability density function equals 1. P is the P-Value for the Correlation Coefficient.

506 ~~In Figure 3, ERA5_Rd exhibits optimal performance in DNF and MF, reflected by NSE and R values~~
507 ~~surpassing 0.9. In these land covers, the mean RMSEs stand at 11 W m⁻², mean RMSEu at 24.5 W m⁻²,~~
508 ~~and mean RMSE at 26.9 W m⁻². However, its performance in SAV is notably subpar, characterized by~~
509 ~~an NSE of 0.29, an R of 0.59, highest RMSEs of 40 W m⁻², RMSEu of 48.9 W m⁻², and RMSE of 63.2~~
510 ~~W m⁻². For ERA5_Rd, the mean RMSEs amount to 16 W m⁻², and the mean RMSEu is 34.8 W m⁻²,~~
511 ~~suggesting that ERA5_Rd demonstrates high accuracy by effectively capturing the systematic variation~~
512 ~~in Obv_Rd, as indicated by its relatively low RMSEs and RMSEu close to RMSE (Willmott et al., 1981)~~
513 ~~in most land covers, except for SAV. Specifically, we have annotated the figure to indicate that all Rd~~
514 ~~values derived from ERA5 exhibit very low P-values (<0.01). This indicates a statistically significant~~
515 ~~correlation between the input shortwave radiation from ERA5 and the local measurements.~~

516 Several factors come into play in understanding the disparities in performance in downward solar
517 radiation of ERA5 (ERA5_Rd) across different land cover types. In regions characterized by denser
518 forests, such as DNF and MF, ERA5_Rd's ~~superior~~ performance may be attributed to the lower
519 density of ground-based meteorology stations (DNF, N = 1096) and the relatively uniform subsurface
520 and canopy coverage in MF, facilitating a more accurate representation in the ERA5 radiative transfer
521 model. Conversely, savannas present unique challenges due to sparse vegetation and flat terrain,
522 influencing sunlight transmission dynamics (Yang and Friedl, 2003). Land-use changes, including
523 farming and urban development, further complicate the accuracy of sunlight transmission (Wang et al.,
524 2014; Zhang et al., 2022). Additionally, factors like aerosols from natural or anthropogenic sources
525 contribute to data variations (Naud et al., 2014; Wang et al., 2021b). The inaccuracies in accounting for
526 the rainy season, leading to increased cloud cover and rainfall in savannas, contribute to ERA5_Rd's
527 limitations (Jiang et al., 2020).

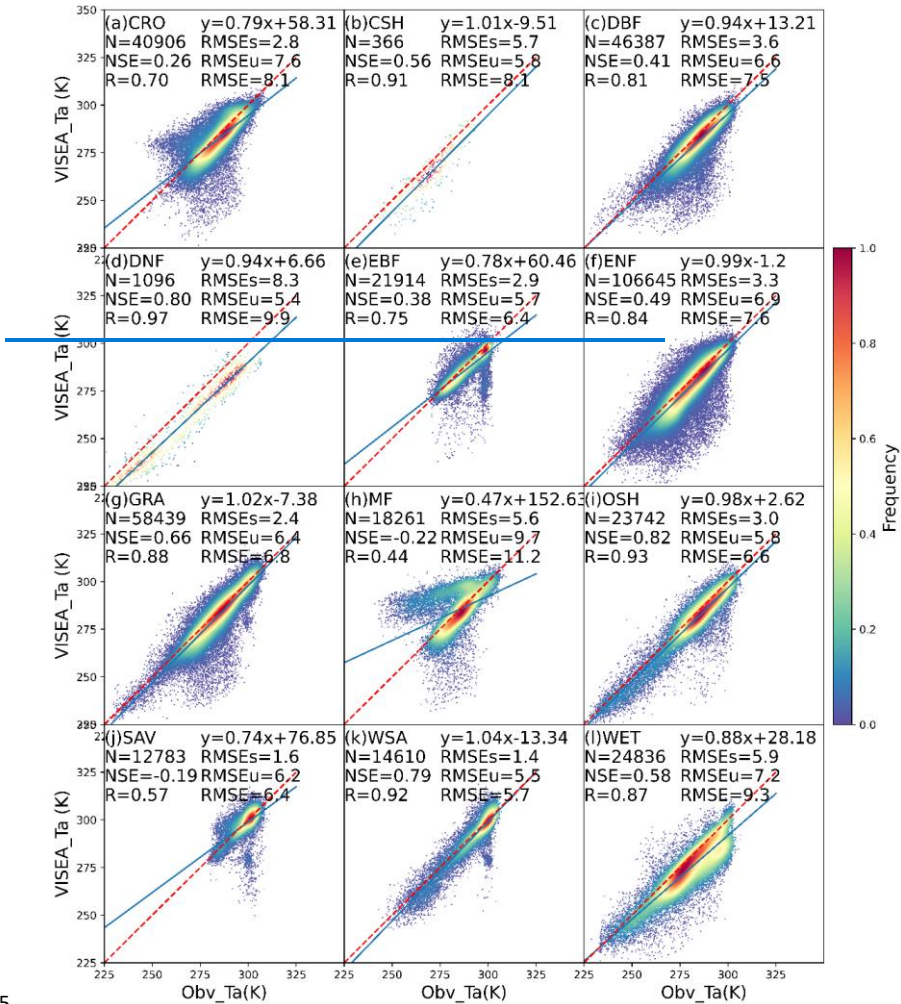
528 ~~Our local scale evaluation, as demonstrated in Figure 3, which is the comparison of ERA5 shortwave~~
529 ~~radiation and Figure 4, the daily air temperature calculated by MODIS land surface and vegetation index~~
530 ~~with the VI Ts method, supports our stance that this resolution disparity between MODIS Land product~~
531 ~~at 0.05° and ERA5 data at 0.1° minimally impacts the final ET product's accuracy. This approach is~~
532 ~~consistent with the methodologies adopted in the studies by Huang et al. (2017, 2021, 2023), which~~
533 ~~effectively utilized MODIS land products at a 0.05° resolution in conjunction with downward shortwave~~
534 ~~radiation data at a 0.1° resolution from the China Meteorology Forcing Dataset. Such precedents~~

535 underscore the feasibility of integrating these resolutions for ET estimation, bolstering our confidence in
536 the methodological integrity of our study despite the noted resolution differences.

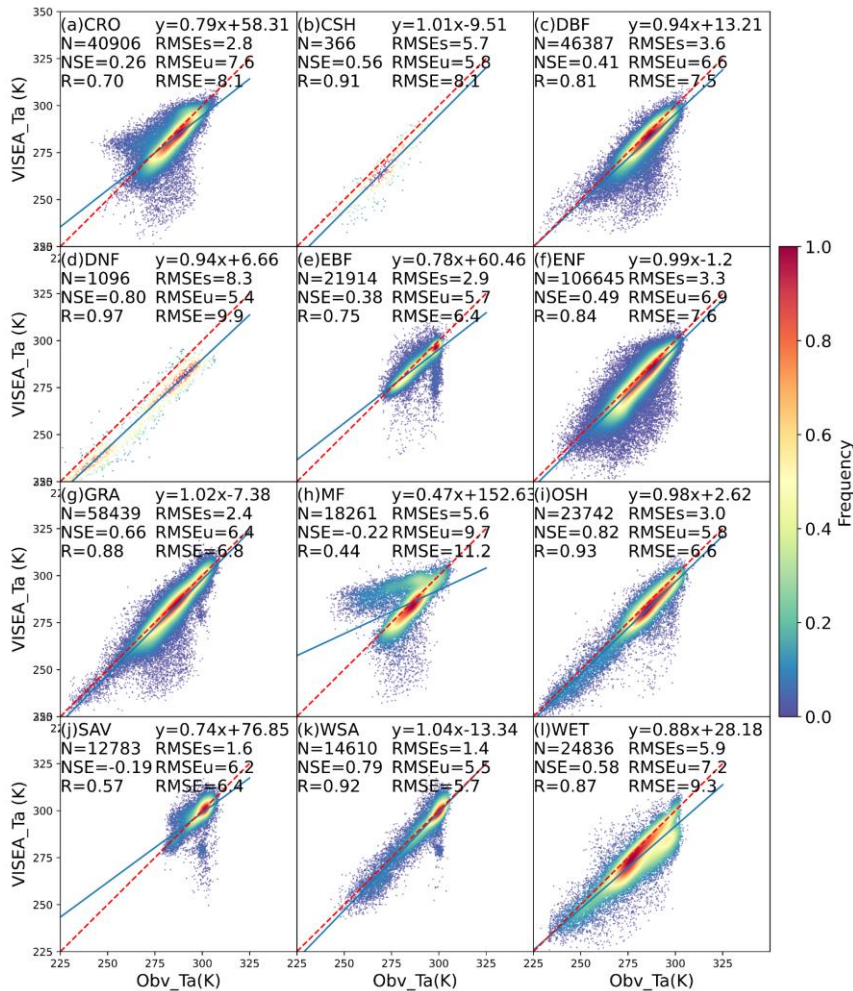
537 We chose to utilize 0.05° MODIS data for its detailed land surface information, daily time step, and
538 global coverage, which is essential for accurate and near-real-time ET calculations. Although ERA5 data
539 is at a coarser 0.1° resolution, it provides necessary atmospheric inputs that can be effectively interpolated
540 to match the MODIS resolution without significant loss of accuracy. As illustrated in Figures 3 and 4,
541 our tests confirm that this method achieves accurate ET despite the resolution differences.

542 Figure 4 depicts scatter plots illustrating the comparison between the estimated air temperature using
543 the VI-T_s method (VISEA_Ta) and local meteorological measurements (Obv_Ta). The analysis reveals
544 that VISEA_Ta generally aligns with Obv_Ta, exhibiting NSE values ranging from -0.22 (MF) to 0.82
545 (OSH), R values ranging from 0.44 (MF) to 0.97 (DNF), and RMSE values ranging from 5.7 K (WSA)
546 to 11.2 K (MF). Particularly noteworthy is VISEA_Ta's outstanding performance at OSH (NSE = 0.82,
547 R = 0.93, RMSE = 6.6 K), WSA (NSE = 0.79, R = 0.92, RMSE = 5.7 K) and GRA (NSE = 0.66, R =
548 0.88, RMSE = 6.8 K). Conversely, the least satisfactory performance is evident at MF (NSE = -0.22, R
549 = 0.44, RMSE = 11.2 K), SAV (NSE = -0.19, R = 0.57, RMSE = 6.4 K), and CRO (NSE = 0.26, R =
550 0.70, RMSE = 8.1 K). The RMSEs are lower than RMSEu in most land cover sites, except in DNF.
551 Despite VISEA_Ta displaying a high NSE of 0.8 and R of 0.97 at DNF, it exhibits higher RMSEs (8.3
552 K) compared to RMSEu (5.4 K), indicating a systematic underestimation of VISEA_Ta at DNF.

553 As detailed in Section 2.4, the VI-Ts method relies on a negative correlation between vegetation coverage
 554 (VI) and land surface temperature (Ts), ideally suited for cases with significant VI and Ts differences.



555
 556 However, the assumed negative correlation breaks down for land cover types like DNF and MF in
 557 temperate regions with distinct seasons and cool-to-cold climates. In these regions, the positive
 558 correlation between VI and Ts, driven by vegetation growth proportional to rising Ts, results in the failure
 559 of the VI-Ts method. The challenges persist in SAV, where the VI-Ts method encounters difficulties
 560 during dry and wet seasons. In the dry season, the method falters due to the prevalence of bare soil,
 561 resulting in VI values approaching zero and homogeneous high Ts values. Conversely, the wet season
 562 presents challenges, with both VI and Ts exhibiting relatively high values and limited variances between
 563 grid cells, ultimately undermining the accuracy of VISEA_Ta estimation.



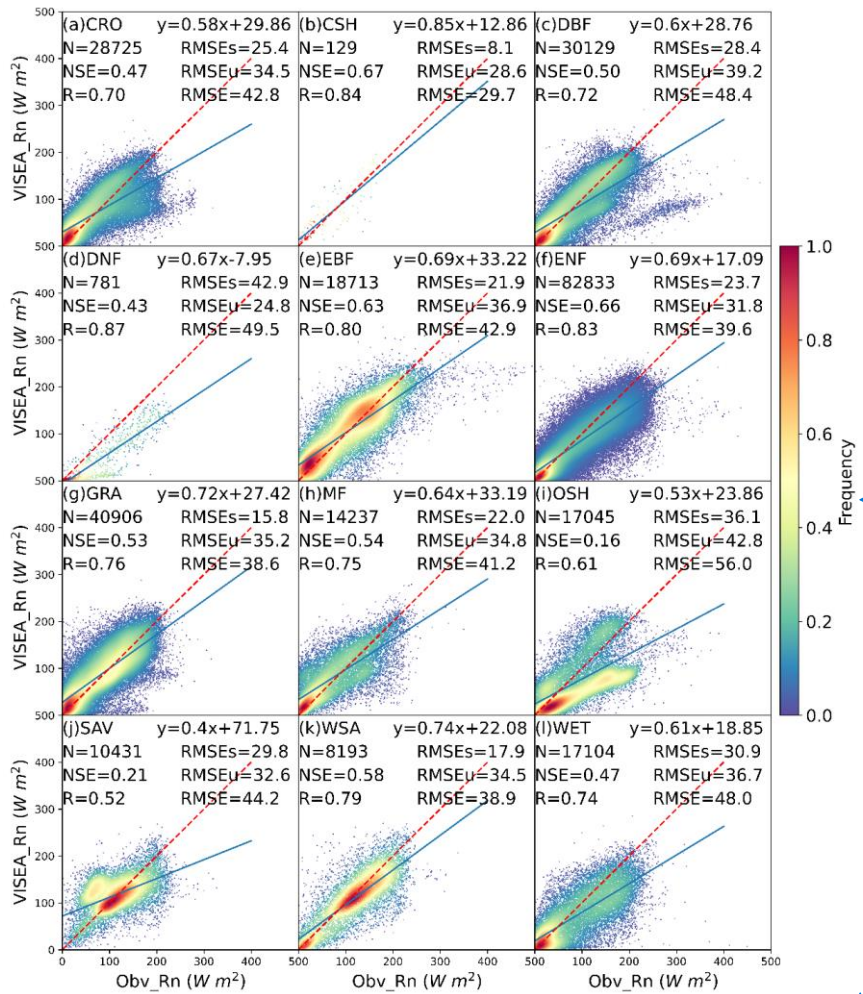
566 **Figure 4.** The scatter plot of daily air temperature simulated by VISEA (VISEA_Ta) compared with local
 567 instruments measurements (Obv_Ta) under 12 IGBP land cover types: CRO (Croplands), CSH (Closed
 568 shrublands), DBF (Deciduous broadleaf forests), DNF (Deciduous needle leaf forests), EBF (Evergreen
 569 broadleaf forests), ENF (Evergreen needle leaf forests), GRA (Grasslands), MF (Mixed forests), OSH
 570 (Open shrublands), SAV (Savannas), WSA (Woody savannas), WET (Permanent wetlands). The red
 571 dotted line is the 1:1 line. N is the number of data points, NSE is Nash-Sutcliffe Efficiency, R is
 572 correlation coefficients, RMSE is Root Mean Square Error, RMSEs is systematic RMSE, and RMSEu is
 573 unsystematic RMSE. The frequency denotes the probability density estimated through the Kernel Density
 574 Estimation, KDE method with a Gaussian kernel, and it is then scaled to ensure that the maximum value
 575 of the probability density function equals 1.

576 ~~Conversely, its least satisfactory performance is evident at MF (NSE = -0.22, R = 0.44, RMSE =~~
577 ~~11.2 K), SAV (NSE = 0.19, R = 0.57, RMSE = 6.4 K), and CRO (NSE = 0.26, R = 0.70, RMSE = 8.1~~
578 ~~K). The RMSEs are lower than RMSEu in most land cover sites, except in DNF. Despite VISEA_Ta~~
579 ~~displaying a high NSE of 0.8 and R of 0.97 at DNF, it exhibits higher RMSEs (8.3 K) compared to~~
580 ~~RMSEu (5.4 K), indicating a systematic underestimation of VISEA_Ta at DNF.~~

581 ~~As detailed in Section 2.4, the VI-Ts method relies on a negative correlation between vegetation~~
582 ~~coverage (VI) and land surface temperature (Ts), ideally suited for cases with significant VI and Ts~~
583 ~~differences. However, for land cover types like DNF and MF situated in temperate regions with distinct~~
584 ~~seasons and cool to cold climates, the assumed negative correlation breaks down. In these regions, the~~
585 ~~positive correlation between VI and Ts, driven by vegetation growth proportional to rising Ts, results in~~
586 ~~the failure of the VI-Ts method. The challenges persist in SAV, where the VI-Ts method encounters~~
587 ~~difficulties during both dry and wet seasons. In the dry season, the method falters due to the prevalence~~
588 ~~of bare soil, resulting in VI values approaching zero and homogeneous high Ts values. Conversely, the~~
589 ~~wet season presents challenges with both VI and Ts exhibiting relatively high values and limited~~
590 ~~variances between grid cells, ultimately undermining the accuracy of VISEA_Ta estimation.~~

591 The simulated daily net radiation (VISEA_Rn) from VISEA is assessed against local meteorological
592 measurements (Obv_Rn) in Figure 5. In contrast to the satisfactory performance of ERA5_Rd in Figure
593 3, VISEA_Rn exhibits more notable discrepancies, characterized by significant underestimation
594 compared to Obv_Rn. This is reflected in the mean NSE of 0.49, mean R of 0.74, and mean RMSE of
595 43.3 W m⁻². Specifically, VISEA_Rn demonstrates good accuracy in certain land cover types, including
596 CHS with an NSE of 0.67, R of 0.84, and RMSE of 29.7 W m⁻², EBF with an NSE of 0.63, R of 0.8, and
597 RMSE of 42.9 W m⁻², and ENF with an NSE of 0.66, R of 0.83, and RMSE of 39.6 W m⁻². However, its
598 performance diminishes notably at OSH, where it records an NSE of 0.16, R of 0.61, and RMSE of 56
599 W m⁻², as well as in SAV, with an NSE of 0.21, R of 0.52, and RMSE of 44.2 W m⁻². While VISEA_Rn
600 appears to have lower accuracy compared to ERA5_Rd, in the majority of land cover types, the RMSEs
601 are smaller than RMSEu, with mean RMSEs of 25.2 W m⁻² and mean RMSEu of 34.3 W m⁻². Moreover,
602 the RMSEu of 43.3 W m⁻² is almost the same as the RMSE.

603 In the context of VISEA_Rn, a consistent pattern of approximately 30% underestimation in net
604 radiation across various land cover types raises noteworthy discussions. This systematic discrepancy
605 could be linked to the disparity in vegetation coverage between the observed sites' footprint and the mean
606 vegetation coverage of the 0.05° × 0.05° grid cell. Specifically, the lower albedo within the footprint,
607 compared to the grid cell's average albedo (as expressed by Eq. 14, contributes to the underestimation of
608 Obv_Rn. This is particularly evident in OSH, where the vegetation coverage within the footprint
609 significantly exceeds the mean vegetation coverage of the grid cell (<0.2 compared to >0.5). Factors such
610 as the bias in ERA5_Rd (refer to Fig. 3i) and VISEA_Ta (refer to Fig. 4j) contribute to the
611 underestimation of VISEA_Rn in SAV. Moreover, a substantial 50% underestimation in DNF results
612 from the underestimated VISEA_Ta (refer to Fig. 4d). These findings suggest that VISEA_Rn demonstrates
613 fewer systematic biases, with unsystematic RMSEu contributing the most to the overall RMSE.4d) leads
614 to a subsequent underestimation of downward long-wave radiation.



616

617 **Figure 5.** The scatter plot of daily net radiation simulated by VISEA (VISEA_Rn) compared with local
 618 instruments measurements (Obsv_Rn) under 12 IGBP land cover types: CRO (Croplands), CSH (Closed
 619 shrublands), DBF (Deciduous broadleaf forests), DNF (Deciduous needle leaf forests), EBF (Evergreen
 620 broadleaf forests), ENF (Evergreen needle leaf forests), GRA (Grasslands), MF (Mixed forests), OSH
 621 (Open shrublands), SAV (Savannas), WSA (Woody savannas), WET (Permanent wetlands). The red
 622 dotted line is the 1:1 line. N is the number of data points, NSE is Nash-Sutcliffe Efficiency, R is
 623 correlation coefficients, RMSE is Root Mean Square Error, RMSEs is systematic RMSE, and RMSEu is
 624 unsystematic RMSE. The frequency denotes the probability density estimated through the Kernel Density
 625 Estimation, KDE method with a Gaussian kernel, and it is then scaled to ensure that the maximum value
 626 of the probability density function equals 1.

带格式的: 段落间距段后: 0 磅

设置了格式: 字体: Times New Roman, 10 磅

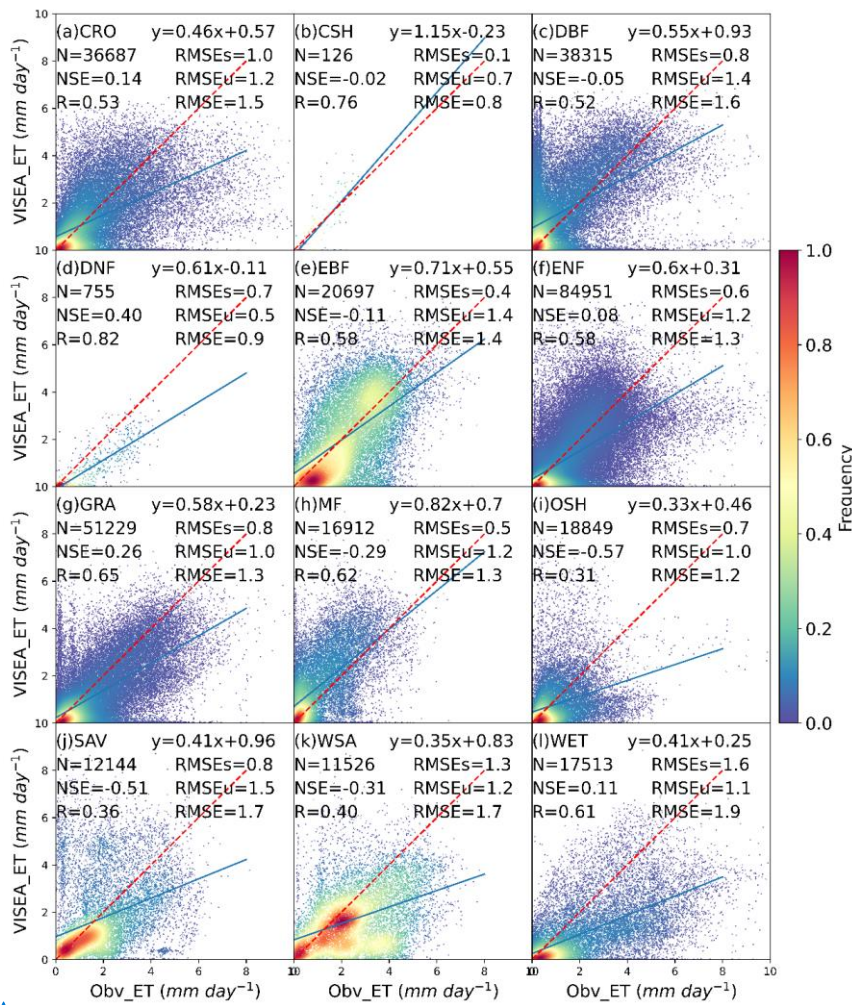
627 In the context of VISEA_Rn, a consistent pattern of approximately 30% underestimation in net
628 radiation across various land cover types raises noteworthy discussions. This systematic discrepancy
629 could be linked to the disparity in vegetation coverage between the observed sites' footprint and the mean
630 vegetation coverage of the $0.05^\circ \times 0.05^\circ$ grid cell. Specifically, the lower albedo within the footprint,
631 compared to the grid cell's average albedo (as expressed by Eq. 14, contributes to the underestimation of
632 Obv_Rn. This is particularly evident in OSH, where the vegetation coverage within the footprint
633 significantly exceeds the mean vegetation coverage of the grid cell (<0.2 compared to >0.5). Additionally,
634 factors such as the bias in ERA5_Rd (refer to Fig. 3, j) and VISEA-Ta (refer to Fig. 4, j) contribute to
635 the underestimation of VISEA_Rn in SAV. Moreover, a substantial 50% underestimation in DNF results
636 from the underestimated VISEA-Ta (refer to Fig. 4, d), leading to a subsequent underestimation of
637 downward long wave radiation. Unpacking these intricacies sheds light on the nuanced interplay of
638 variables influencing the observed underestimation trends in VISEA_Rn across diverse land cover types.

639 Figure 6 illustrates scatter plots of daily evapotranspiration (ET) simulated by VISEA (VISEA_ET)
640 against eddy covariance measurements obtained from 149 flux tower sites (Obv_ET) across 12 IGBP
641 land cover types. The scatter plots of VISEA_ET reveal a dispersed distribution, as evidenced by an
642 average NSE of -0.08, average R of 0.56, and average RMSE of 1.4 mm day^{-1} . Notably, VISEA_ET tends
643 to underestimate daily ET across most land cover types. Among the 12 land cover types, VISEA_ET
644 exhibits the highest accuracy in DNF, with an NSE of 0.4, an R of 0.82, and an RMSE of 0.9 mm day^{-1} .
645 It was closely followed by GRA, with NSE values of 0.26, R values of 0.65, and RMSE values of 1.3
646 mm day^{-1} . However, for CRO, ENF, and WET land cover types, the NSE values, although above 0, are
647 close to 0 (mean NSE of 0.11), with a mean R of 0.53 and a mean RMSE of 1.3 mm day^{-1} . In the remaining
648 land cover types, particularly in OSH and SAV, VISEA_ET appears to struggle in aligning with local
649 measurements, resulting in NSE values of -0.57 and -0.51, R values of 0.31 and 0.36, and RMSE values
650 of 1.2 mm day^{-1} and 1.7 mm day^{-1} , respectively. As the evaluation of daily VISEA_ET with observed
651 ET, Obv_ET, at CRO and WET, the bias mainly ~~comes~~ comes from the bias in ERA5_Rd (the third highest
652 RMSE of 45.2 W m^{-2} and second highest RMSE of 59.4 W m^{-2}) (Fig. 3, a3a and l). In ENF, the biases
653 primarily ~~could be~~ caused by the disability of VISEA_ET to ~~capture~~ capturing the Obv_ET under a cold
654 climate, with low net radiation estimation (Fig. 5, f, 5f) and air temperature (Fig. 4, f, 4f). For OSH, the
655 bias mainly arises from the poor estimation of VISEA_Rn, which has the lowest NSE of 0.16 and the
656 highest RMSE of 56 W m^{-2} (Fig. 5, i5i). The bias of VISEA_ET in SAV is a result of the combined biases
657 in ERA5_Rd (the lowest NSE and R of 0.29 and 0.59, respectively, and the highest RMSE of 63.2 W m^{-2}),
658 VISEA-Ta (the second lowest NSE and R of -0.19 and 0.57-, respectively).

659
660
661 The periods when MODIS land temperature data were missing, primarily due to cloud cover,
662 accounted for approximately one-third of the observation period. Using the gap-filling method (section
663 2.3), it can be observed that for most surfaces, the accuracy of VISEA was not significantly affected by
664 clouds, as evidenced by the figures below. The accuracy on cloudy days is slightly lower for some

带格式的: 首行缩进: 2 字符

665 surfaces compared to clear days. For example, in the case of DBF, the correlation coefficient R is 0.52
 666 on both clear and cloudy days, and the RMSE is 1.4 mm day⁻¹ on both clear and cloudy days, indicating
 667 a slight decrease in accuracy under cloudy conditions. Similarly, for ENF, the R value is 0.59 on clear
 668 days and 0.56 on cloudy days. At the same time, the RMSE is 1.3 mm day⁻¹ on clear days and 1.4 mm
 669 day⁻¹ on cloudy days, showing that although there is some impact, the overall performance of VISEA
 670 remains robust across different weather conditions (Figures S4 and S5).

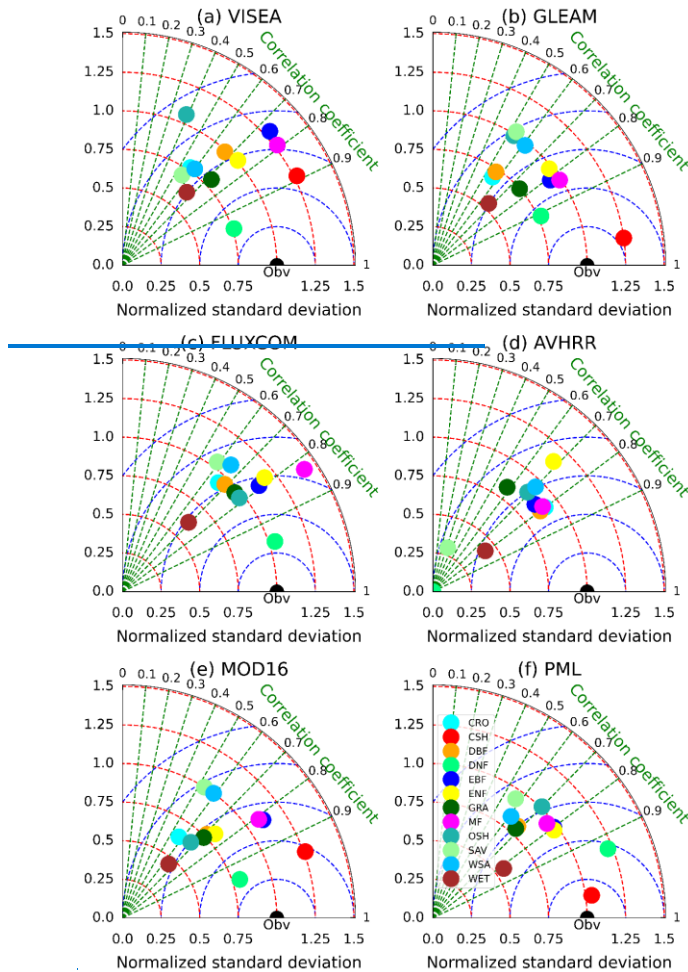


671
 672 **Figure 6.** The scatter plot of daily ET simulated by VISEA (VISEA_ET) compared with local instruments
 673 measurements (Obsv_ET) under 12 IGBP land cover types: CRO (Croplands), CSH (Closed shrublands),
 674 DBF (Deciduous broadleaf forests), DNF (Deciduous needle leaf forests), EBF (Evergreen broadleaf
 675 forests), ENF (Evergreen needle leaf forests), GRA (Grasslands), MF (Mixed forests), OSH (Open
 676 shrublands), SAV (Savannas), WSA (Woody savannas), WET (Permanent wetlands). The red dotted line

677 is the 1:1 line. N is the number of data points, NSE is Nash-Sutcliffe Efficiency, R is correlation
678 coefficients, RMSE is Root Mean Square Error, RMSEs is systematic RMSE, and RMSEu is
679 unsystematic RMSE. The frequency denotes the probability density estimated through the Kernel Density
680 Estimation, KDE method with a Gaussian kernel, and it is then scaled to ensure that the maximum value
681 of the probability density function equals 1.

682 [We also conducted the VISEA sensitivity to different radiation input data by comparing results](#)
683 [obtained using CERES and ERA5 datasets. Specifically, we analyzed the performance of the VISEA](#)
684 [model in simulating net radiation \(Rn\) and evapotranspiration \(ET\), comparing these simulations with](#)
685 [ground-based observational data. Figures S1 and 2 compare the downward shortwave radiation data from](#)
686 [CERES and ERA5 with ground-based observations of the 149 flux towers. The CERES shortwave](#)
687 [radiation data generally agree with the observational data, with a mean R of 0.89, a mean RMSE of 34.8](#)
688 [W m², and a mean NSE of 0.78. In contrast, the ERA5 shortwave radiation data mean R of 0.85, a mean](#)
689 [RMSE of 40.4 W m², and a mean NSE of 0.58 when compared with the ground-based observations,](#)
690 [indicating systematic bias and lower precision for the ERA5 net radiation compared with CERES. Figures](#)
691 [S2 and 5 compare the net radiation of the flux towers with that calculated by the VISEA model with](#)
692 [shortwave radiation of CERES and ERA5 as input data. For CERES data, the mean R is 0.74, the mean](#)
693 [RMSE is 34.3 W m² and the mean NSE is 0.64. The ERA5 data yield a mean R of 0.64, a mean RMSE](#)
694 [of 39.44 W m², and a mean NSE of 0.44. Finally, the ET calculated with the VISEA using the net radiation](#)
695 [of CERES and ERA5 as input is compared with ground-based data in Figures S3 and 6. Again, CERES](#)
696 [outperforms ERA5 as indicated by the statistical measures. The sensitivity analysis reveals that the](#)
697 [VISEA model's performance highly depends on the quality of the incident radiation data used as input.](#)
698 [The model shows better accuracy and consistency with CERES data than ERA5 data. Therefore, selecting](#)
699 [high-precision radiation data is crucial for improving the accuracy and reliability of VISEA model](#)
700 [simulations.](#)

701 In Figure 7, we utilized Taylor diagrams (Taylor, 2001) to evaluate the performances of six global
702 gridded monthly ET products with simulated ET from VISEA (a), GLEAM (b), FLUXCOM (c), AVHRR
703 (d), MOD16 (e), and PML (f). Table 3 lists [the](#) statistical metrics, including correlation coefficient (CC),
704 bias, RMSE, RMSEu, RMSEs, and Nash-Sutcliffe Efficiency (NSE) across different vegetation types
705 and their mean values. The vegetation types include Croplands (CRO), Closed Shrublands (CSH),
706 Deciduous Broadleaf Forest (DBF), Deciduous Needleleaf Forest (DNF), Evergreen Broadleaf Forest
707 (EBF), Evergreen Needleleaf Forest (ENF), Grasslands (GRA), Mixed Forests (MF), Open Shrublands
708 (OSH), Savannas (SAV), Woody Savannas (WSA), Wetlands (WET), and an overall mean (MEAN).

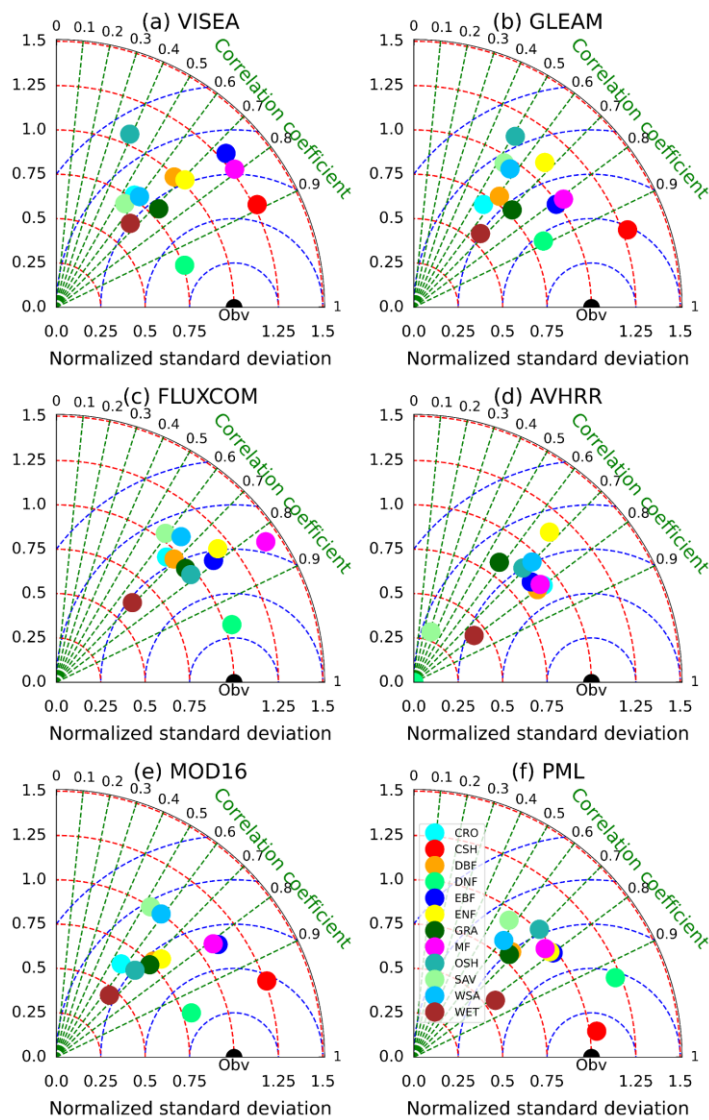


709

710 [VISEA](#), with a mean correlation coefficient (CC) of 0.69, indicates moderate correlation across
 711 [vegetation types](#) but suffers from significant biases, notably in WET, with a mean bias of -9.56
 712 [mm month⁻¹](#). It also has the highest mean Root Mean Square Error (RMSE) at 31.6 mm month⁻¹ and a mean
 713 [NSE of 0.25](#). MOD16 demonstrates a slightly better correlation with a mean CC of 0.72 and presents less
 714 [variation in bias](#), resulting in a marginally lower mean RMSE of 28.7 mm month⁻¹ and a higher mean
 715 [NSE of 0.36](#). AVHRR matches VISEA in mean CC at 0.69 but exhibits extreme biases, particularly in
 716 [SAV](#), and achieves a comparable mean RMSE of 26.3 mm month⁻¹. However, its mean NSE of 0.10 is
 717 [the lowest among the six products](#), suggesting its predictions are less reliable.

718 [On the other hand](#), GLEAM, FLUXCOM, and PML show better agreements. GLEAM has a high
 719 [mean CC of 0.69](#) with the lowest bias at -0.82 mm month⁻¹, indicating consistent performance with a
 720 [mean RMSE of 29.6 mm month⁻¹](#) and a mean NSE of 0.31. FLUXCOM exhibits a higher mean CC of
 721 [0.76](#), suggesting better overall correlation, but with a higher mean bias of 6.2 mm month⁻¹, it hints at a

722 tendency towards overestimation. The mean RMSE is 30.0 mm month⁻¹, with a mean NSE of 0.22. PML
 723 outperforms the others, with the highest mean CC of 0.75 and the highest mean NSE of 0.49, indicating
 724 the strongest predictive accuracy. It also has the lowest mean RMSE at 26.0 mm month⁻¹.



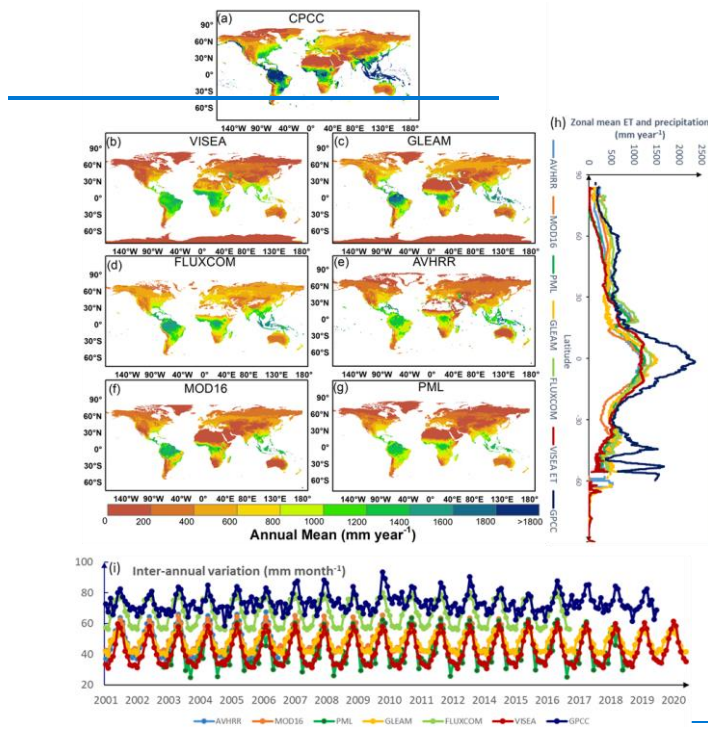
725
 726 **Figure 7.** Taylor Diagrams comparing monthly measurements of (a) VISEA, GLEAM (b), FLUXCOM
 727 (c), AVHRR (d), MOD16 (e), and PML (f) with 15 flux towers (labeled as Obv) in different IGBP land
 728 cover types. The diagrams display the Normalized Standard Deviation (represented by red circles),
 729 Correlation Coefficient (shown as green lines), and Centred Root-Mean-Square (depicted as blue circles).

738 variation in bias, resulting in a marginally lower mean RMSE of 28.7 mm month⁻¹ and a higher mean
739 NSE of 0.41. AVHRR matches VISEA in mean CC at 0.69 but exhibits extreme biases, particularly in
740 SAV, and achieves a comparable mean RMSE of 31.5 mm month⁻¹. However, its mean NSE of 0.12 is
741 the lowest among the six products, suggesting its predictions are less reliable.

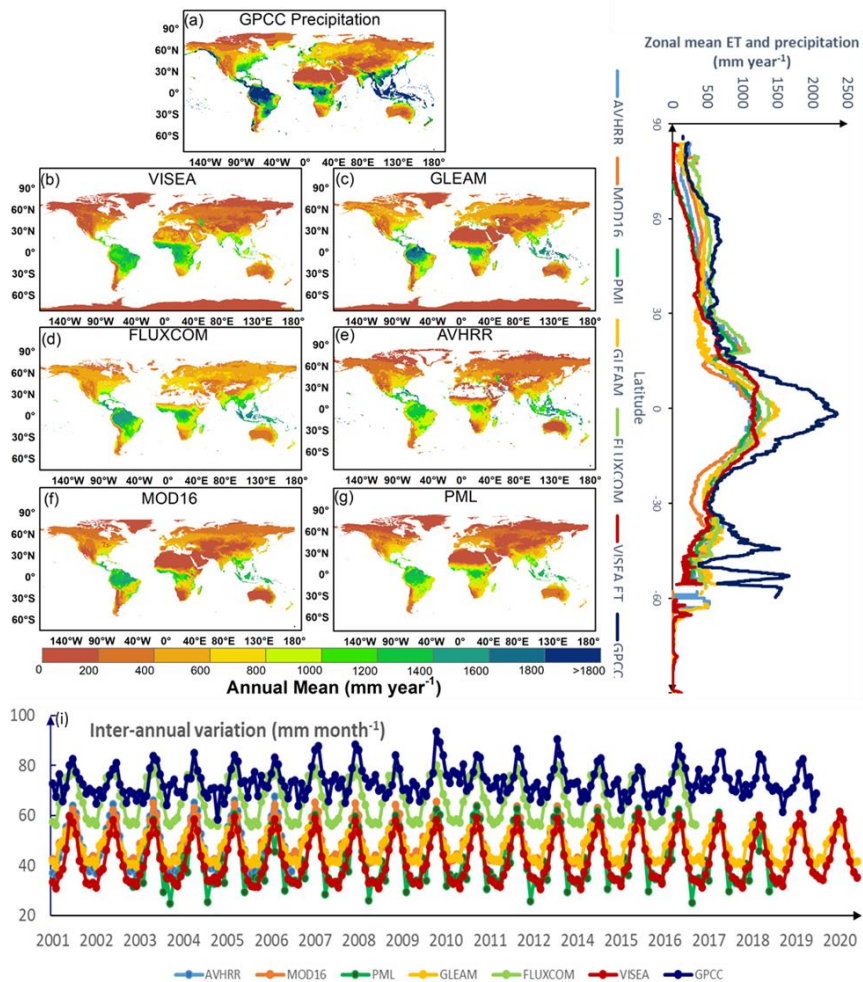
742 On the other hand, GLEAM, FLUXCOM, and PML show better agreements. GLEAM has a high
743 mean CC of 0.71 with the lowest bias at -1.66 mm month⁻¹, indicating a consistent performance with a
744 mean RMSE of 28.3 mm month⁻¹ and a mean NSE of 0.38. FLUXCOM exhibits a higher mean CC of
745 0.76, suggesting better overall correlation, but with a higher mean bias of 6.1 mm month⁻¹, it hints at a
746 tendency towards overestimation. The mean RMSE stands at 29.9 mm month⁻¹, with a mean NSE of 0.22.
747 PML outperforms the others with the highest mean CC of 0.75 and the highest mean NSE of 0.49,
748 indicating the strongest predictive accuracy. It also has the lowest mean RMSE at 25.9 mm month⁻¹,
749 affirming its status as the most accurate ET estimation product among those evaluated.

750 Figure 8 illustrates the spatial distribution of the multi-year average (a-g), the zonal mean (h) and
751 inter-annual variation (i) of (a) GPCC (2001-2019), (b) VISEA (2001-2020), (c) GLEAM (2001-2020),
752 (d) FLUXCOM (2001-2016), (e) AVHRR (2001-2006), (f) MOD16 (2001-2014) and (g) PML (2003-
753 2018).

754



755



756
 757 **Figure 8.** The spatial distribution of the multi-year average (a-g), the zonal mean (h) and inter-annual
 758 variation (i) of (a) GPCC [precipitation](#) (2001-2019), (b) VISEA (2001-2020), (c) GLEAM (2001-2020),
 759 (d) FLUXCOM (2001-2016), (e) AVHRR (2001-2006), (f) MOD16 (2001-2014) and (g) PML (2003-
 760 2018)-) [ET data](#).

761 The VISEA ET product demonstrates consistent spatial distribution patterns among the six ET
 762 products across various years, both in terms of annual means (a-g) and latitude-zonal means (h). These
 763 patterns align closely with the precipitation distribution data from GPCC. It also exhibits similar
 764 distributions to other ET products, both below the 5th percentile (Figure S4) and above the 95th percentile
 765 (Figure S5). The highest ET values (about 1,500 mm year⁻¹) are predominantly concentrated in equatorial
 766 low-latitude regions with the highest precipitation levels (nearly 2,500 mm year⁻¹). The available water
 767 for evaporation and transpiration is abundant, and the primary constraint on evapotranspiration lies in the
 768 availability of energy to drive the process. In such conditions, water availability is not a limiting factor,

带格式的: 缩进: 首行缩进: 2 字符

769 allowing for ample potential evapotranspiration. These regions include South America (Amazon Basin),
770 Central Africa (Congo Basin), and Southeast Asia (encompassing Indonesia, Malaysia, parts of Thailand,
771 and the Philippines), which are known for their tropical rainforest climates. These ET estimates align
772 with the findings of Chen et al. (2021) and Zhang et al. (2019) who reported that the multi-year average
773 annual ET is nearly 1,500 and the precipitation is approximately 2,500 mm year⁻¹ (Panagos et al., 2017).
774 in terms of annual means (a-g) and latitude zonal means (h). These patterns closely align with the
775 precipitation distribution data from GPCC. Furthermore, VISEA ET also exhibit similar spatial
776 distributions compared to other ET products, particularly in the extremes of the distribution, below the
777 5th percentile and above the 95th percentile (Figure S6, S7). The highest ET values, approximately 1,500
778 mm year⁻¹, are predominantly in equatorial low-latitude regions with the corresponding high precipitation
779 levels of approximately 2,500 mm year⁻¹. These regions include South America (Amazon Basin), Central
780 Africa (Congo Basin), and Southeast Asia (encompassing Indonesia, Malaysia, parts of Thailand, and the
781 Philippines), which have tropical rainforest climates. Remote sensing data support the ET estimates and
782 align with findings from previous studies, such as Chen et al. (2021) and Zhang et al. (2019), who reported
783 that the multi-year average annual ET is nearly 1,500 and the precipitation is approximately 2,500 mm
784 year⁻¹. Also, Panagos et al. (2017) report similar multi-year average annual ET and precipitation rates.

设置了格式: 英语(美国)

785 Conversely, areas categorized as In this analysis, barren landlands (BAR), including deserts) such as
786 the Sahara, Arabian, Gobi, and Kalahari, and deserts, along with large portions areas of Australia, as well
787 as and snow and ice (SI) areas like most regions including significant parts of Canada, Russia, and the
788 Qinghai-Tibet Plateau in China, where the growing seasons are short, typically falling below 400 mm
789 year⁻¹. These areas are also are characterized by the lowest notably low evapotranspiration (ET). These
790 regions typically experience less than 400 mm year⁻¹ of annual ET, paralleled by minimal yearly
791 precipitation, ranging from 200 to 400 mm year⁻¹, according to GPCC precipitation data mm year⁻¹.
792 Comparative ET estimates rates for other land cover types fall within this generally range, varying
793 from 400 to 1,400 mm year⁻¹, in close alignment with closely following the GPCC precipitation data, which
794 falls between amounts of 600 to 1,600 mm year⁻¹. In these areas, there is a surplus of available energy,
795 and the primary limitation on ET stems from the availability of water. This implies a high atmospheric
796 water demand, often quantified as potential evapotranspiration (potential ET).

797 In regions with experiencing moisture-limited evapotranspiration (ET), the primary constraint on ET
798 arises from the limited availability scarcity of water. These areas typically experience insufficient
799 precipitation or water supply, leading to a situation where the atmospheric demand for moisture exceeds
800 the available water resources. On the other hand, regions with is the primary constraint. Conversely, in
801 areas where sufficient water is available, ET is energy-limited ET face limitations due to inadequate
802 energy for the process of evaporation, and transpiration. This can be influenced by factors such as cloud
803 cover, or shading, or other conditions that limit restrict the absorption of solar radiation. In such areas,
804 even if there is an ample water supply, the lack of sufficient energy hinders the rate of, affecting the
805 evapotranspiration rate. Panel (i) in Figure 8 illustrates inter-annual monthly variations over the past two
806 decades. It shows how VISEA and other satellite-based ET products, alongside GPCC precipitation data,
807 capture the rhythmic patterns of ET. These data reveal distinctive seasonal fluctuations and highlight the

设置了格式: 英语(美国)

设置了格式: 英语(美国)

设置了格式: 英语(美国)

设置了格式: 英语(美国)

设置了格式: 英语(美国)

设置了格式: 英语(美国)

设置了格式: 英语(美国)

设置了格式: 英语(美国)

设置了格式: 英语(美国)

设置了格式: 英语(美国)

设置了格式: 英语(美国)

设置了格式: 英语(美国)

带格式的: 缩进: 首行缩进: 2 字符

808 [significant inter-annual climate variability. Among these products, FLUXCOM consistently shows ET](#)
809 [values 10-20 mm month⁻¹ higher than those of other ET products. GLEAM and MOD16 exhibit similar](#)
810 [ET estimations, closely paralleling each other, as do PML and VISEA. Notably, after 2007, both GLEAM](#)
811 [and MOD16 reported higher ET estimations than PML and VISEA in November, December, January,](#)
812 [and February. For the same months, PML consistently records lower ET estimations than VISEA.](#)

813 [Analysis across the datasets reveals how ET estimates respond to extreme climate events, providing](#)
814 [insights into the variability and resilience of these models. For instance, during the 2011-2012 drought in](#)
815 [the Horn of Africa—one of the most severe droughts in recent decades—both ET estimations and GPCC](#)
816 [precipitation data showed significant declines. Similarly, the prolonged California drought from 2012 to](#)
817 [2016 also saw a considerable decrease in ET values, aligning with the reduced precipitation levels](#)
818 [captured by GPCC.](#)

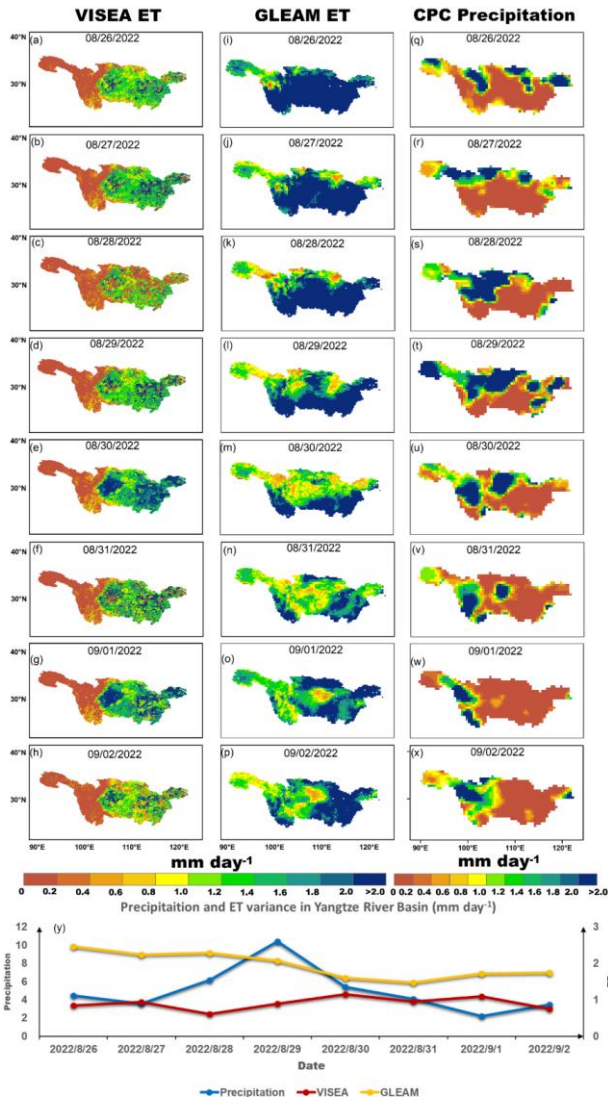
819 Regarding the inter-annual monthly variations, panel (i) shows the fluctuations in ET across
820 different years for the analyzed ET products and precipitation data. The graph reveals a rhythmic pattern
821 of ET across the years. VISEA ~~with~~ and other ET products showed distinctive peaks and troughs ~~that~~
822 ~~correspond~~ [corresponding](#) to seasonal changes and inter-annual climate variability. The ET products' data
823 ~~exhibit a close alignment~~ [align closely](#) with the precipitation patterns reported by GPCC, highlighting the
824 interconnectedness between ET and precipitation as climatic variables. Notably, FLUXCOM consistently
825 presents higher ET estimations ~~compared to~~ [than](#) the other products, ~~and~~ GLEAM's ET estimations are
826 also slightly higher during the winter, indicating a trend of systematic overestimation in these products
827 relative to the others in the dataset.

828 [Figure 9 presents the daily variations in ET from VISEA and GLEAM along with the precipitation](#)
829 [from Global Unified Gauge Based Analysis of Daily Precipitation recorded in the Yangtze River Basin](#)
830 [during from August 26th, 2022, to September 2nd, 2022. According to a study by Zhang et al. \(2023\), the](#)
831 [Yangtze River Basin endured a significant drought during the summer of 2022, beginning in July and](#)
832 [showing signs of abatement towards the end of August and into early September. As GLEAM failed to](#)
833 [capture the variability of ET during this drought and exhibited a negative correlation with precipitation](#)
834 [data from CPC, we wouldn't discuss it further in this context.](#)

835 [Figure 9 presents the daily ET from VISEA and GLEAM, alongside precipitation data from the](#)
836 [GPCC across the Yangtze River Basin from August 26th to September 2nd, 2022. During this period, a](#)
837 [significant drought was observed in the region, which began in July and showed signs of abating by late](#)
838 [August and early September, according to Zhang et al. \(2023\). VISEA ET illustrates the evolving drought](#)
839 [conditions, with notably low ET levels \(below 1 mm day⁻¹\) across the basin from August 26th to 28th, as](#)
840 [shown in panels \(a-c\). A marked increase in precipitation on August 29th, evident in panels \(s\) and \(u\),](#)
841 [correlates with an uptick in ET values \(surpassing 1 mm day⁻¹\) throughout the basin, visualized in panels](#)
842 [\(d-f\). Although GLEAM generally captures the fluctuations in ET—both decreases and increases—](#)
843 [during this period, it consistently reports much higher ET values than VISEA. The panel \(v\) graph in](#)
844 [Figure 9 shows the precipitation and the ET calculated by VISEA and GLEAM after an 11 mm rainfall](#)
845 [on August 29th. The ET of VISEA increased and the decreased, which is expected because ET and soil](#)

846 [moisture are positively correlated. The GLEAM does not follow the expected pattern shown in panel y.](#)
847 [This comprehensive analysis highlights the interdependence of precipitation and ET and underscores the](#)
848 [importance of considering soil moisture dynamics to fully understand the hydrological processes within](#)
849 [the Yangtze River Basin during extreme weather events.](#)

850 [Beyond precipitation, soil moisture is a critical regulator of ET, particularly during droughts and](#)
851 [their recovery phases. Acting as a buffer, soil moisture tempers ET rates during dry periods and amplifies](#)
852 [them after rainfall, as noted in late August. This buffering capacity results in a delay between precipitation](#)
853 [events and subsequent ET changes, which is key to understanding drought recovery dynamics. VISEA's](#)
854 [data accurately reflect these variations in precipitation, demonstrating its effectiveness in tracking daily](#)
855 [ET fluctuations and its reliability for near-real-time monitoring of ET during hydrological extremes.](#)



856

857 **Figure 9.** Daily ET from VISEA (a-h), GLEAM (i-p), and CPC precipitation (q-x) distributions from
 858 August 26th to September 2nd in 2022, alongside daily mean ET and Precipitation variances in the Yangtze
 859 River Basin (y) during the same period.

860 VISEA ET graphically illustrates the evolving drought conditions: with notably low ET levels (below
 861 1 mm day⁻¹) across the basin on August 26th to 28th, evidenced in panel (a-c). A notable increase in
 862 precipitation on August 29th, reflected in panels (s) and (u), correlates with an upswing in ET values
 863 (surpassing 1 mm day⁻¹) throughout the basin, as visualized in panels (d-f). The graph in panel (y) displays
 864 the variances in mean ET and precipitation within the basin over this timeframe, highlighting a significant

设置了格式: 字体: 10 磅

865 rise in ET (up to 11 mm day⁻¹) on August 30th, which corresponds with the observed increase precipitation
866 (reaching 11 mm day⁻¹) on August 29th.

867 VISEA's ET data align closely with the variances observed in the CPC precipitation data, showcasing
868 its effectiveness in capturing daily ET fluctuations, especially during and after the drought conditions. It
869 accurately reflects the dip and subsequent recovery in ET values following the precipitation events,
870 indicating its robustness in near-real-time monitoring of ET during such hydrological extremes.

871 5. Discussion

872 While global ET products require at least 2 weeks (GLEAM, FLUXCOM, AVHRR, MOD 16 and
873 PML ET products has more than one years' delay, MOD16 has) require at least 2 weeks delay) to generate
874 global actual ET estimation, we developed VISEA, a satellite-based algorithm which is capable of
875 generating near-real-time evapotranspiration on a daily time step with a resolution of 0.05°. Compared
876 with the monthly global ET of GLEAM, FLUXCOM, AVHRR which have more than two years' delay
877 and 8 day of MOD16 and PML which has more than two weeks' delay and also more than one years'
878 delay. This algorithm is based Nishida et al. (2003) satellite based evaporation fraction algorithm. To
879 assess its accuracy, we compared the calculated ET with data from 149 flux towers around the world in
880 various land use types.

881 Scale mismatch is a problem for many satellite-based ET products. The footprints of these flux towers
882 typically range from 100 to 200 meters, while the VISEA model outputs gridded cells at a resolution of
883 0.05° × 0.05° (nearly 25 km²). This discrepancy introduces errors, especially since flux towers require a
884 uniform fetch, which may not represent the larger gridded cell (Sun et al., 2023). To enhance the validity
885 of our assessments, we assessed monthly values and spatial patterns of our ET measurements with five
886 other satellite-based ET products named MOD16, AVHRR, GLEAM, FLUXCOM and PML
887 (Figure Figures 7 and 8).

888 The evapotranspiration is calculated with VISEA using model uses gridded ERA5-Land shortwave
889 downwards downward radiation, and intermediate variables including as its energy input. Utilizing this
890 input, along with MODIS land surface products, VISEA calculates gridded daily air temperature and net
891 radiation. These two important intermediate variables are essential for estimating daily ET. The
892 calculated evapotranspiration ET generally matches local measurements and other model-calculated
893 values well, but we found significant biases (Figures 6 and 7). These biases largely arise from
894 inaccuracies in the input ERA5-Land shortwave radiation (Figure 3), improper application of the VI-Ts
895 method (Figure 4), and uncertainties in daily net radiation (Figure 5). Below Next, we detail look further
896 into the origin causes of the biases.

897 Incoming shortwave radiation from ERA5-Land is employed to derive the available energy for
898 vegetation coverage and bare soil (Eq. 4415 and 4516), which are the main parameters for calculating
899 daily ET (Eq. 4617). While ERA5-Land is widely utilized as a reanalysis dataset, offering near-real-time
900 land variables by integrating model data with global observations based on physical laws. However, the
901 accuracy of shortwave radiation from ERA5-Land seems compromised in savannas (Figure 3) due to the

设置了格式: 英语(美国)

设置了格式: 英语(美国)

设置了格式: 英语(美国)

设置了格式: 英语(美国)

设置了格式: 英语(美国)

902 challenges associated with simulating radiation transmission under land-use changes and aerosol
903 pollution from natural or anthropogenic sources (Babar et al., 2019; Martens et al., 2020).

904 Air temperature is an important parameter in determining the daily evaporation fraction of bare soil
905 (Appendix B), canopy surface resistance, aerodynamic resistance of the bare soil (Appendix D) and C),
906 atmospheric emissivity (Appendix E-D), and available energy for vegetation coverage and bare soil (Eq.
907 14 and 15). Since air temperature is not measured directly by satellites, many other ET ~~product~~ products
908 use therefore ground observations, land ~~model~~ models or reanalysis data. In contrast, VISEA derives the
909 air temperature from the negative linear relationship between vegetation index (VI) and surface
910 temperature (Ts) using the VI-Ts method (section 2.1.3). It gives very good results under grass land, open
911 shrubland and woody savannas landcover types, as shown in Figure 4. As previously explained, the VI-
912 Ts method relies on the negative linear correlation between the Vegetation Index (VI) and surface
913 temperature (Ts) within a 5 × 5 grids' window. Therefore, ~~both~~ the variance of VI values across these
914 grid cells and the ~~strength of their~~ negative correlation are ~~essential~~ crucial for ~~accurately calculating the~~
915 air temperature (Nishida et al., 2003). However, ~~the VI-Ts method is less effective in regions like dense~~
916 ~~forests, bare lands and deserts, where the vegetation index and temperature data in adjacent grid cells~~
917 ~~show small variations, such as dense forests and bare lands and deserts vary little across the 5 × 5 grids'~~
918 ~~window~~. Also, in regions with freezing temperatures, the VI-Ts method does ~~not~~ perform well, because
919 warmer temperature is related to increased vegetation, ~~which is the~~ opposite ~~the other region~~ of warmer
920 areas, where there is a positive correlation between the vegetation index and surface temperature (Cui et
921 al., 2021).

922 Another bias source of the VISEA model is the uncertainties of daily net radiation, notably
923 originating from input downward shortwave radiation from ERA5-Land (Figure 2) and VI-Ts estimated
924 air temperature (Figure 4). The energy budget equation (Eq. 114) and these two figures indicate that net
925 radiation shows more uncertainties than shortwave radiation and air temperature. At the same time,
926 assuming a linear relationship between cloud coverage (Eq. 1215 and 1316) and ~~the calculation of~~
927 ~~downward~~ calculating downward longwave radiation (Eq. 1417 and 1518) may be an oversimplification
928 that could introduce uncertainties. Since available energy for evapotranspiration (ET) depends on net
929 radiation (Eq. 1614), addressing these uncertainties is crucial for enhancing overall model accuracy
930 (Brutsaert, 1975; Huang et al., 2023). Future refinements will contribute to a more precise daily net
931 radiation estimation within the VISEA model.

932 The VISEA model calculates ET primarily based on vegetation coverage, utilizing it as an indirect
933 constraint to estimate evapotranspiration. However, this model does not directly incorporate variables
934 related to water availability, which is a critical factor in ET processes. In tropical regions, where ~~there is~~
935 ~~an abundance of~~ solar radiation ~~is abundant~~ (available energy), the model tends to overestimate ET due
936 to its emphasis on vegetation coverage without adequately accounting for the actual water available for
937 evapotranspiration. This methodology, while ~~effective~~ ~~ineffectively~~ capturing the ~~influeence~~ effect of
938 vegetation on ET under varied conditions, can lead to overestimations in areas where energy availability
939 significantly exceeds water availability, typical of many tropical regions. Our analysis and subsequent

带格式的: 缩进: 首行缩进: 2 字符

设置了格式: 英语(美国)

设置了格式: 英语(美国)

设置了格式: 英语(美国)

设置了格式: 英语(美国)

设置了格式: 英语(美国)

设置了格式: 英语(美国)

设置了格式: 英语(美国)

设置了格式: 英语(美国)

设置了格式: 英语(美国)

设置了格式: 英语(美国)

940 discussion aim to highlight this characteristic of the VISEA model, acknowledging its implications for
941 ET estimations in such energy-rich, water-variable environments.

942 ~~Furthermore, While the VISEA model exhibits~~ provides evapotranspiration (ET) globally, its best ET
943 ~~is between 60°N and 90°S, as evidenced by a tendency~~ Nash-Sutcliffe efficiency (NSE) of 0.4 and a
944 ~~correlation coefficient (R) of 0.9 in Figure 6. VISEA model tends~~ to underestimate ET in colder regions
945 within the 60°N to 90°~~N~~ latitude range, such as the western territories of Canada. This underestimation
946 is primarily due to the model's inability to incorporate evaporation from frozen surfaces into its ET
947 calculations. These discrepancies arise from several factors: inaccuracies in the ERA5-Land shortwave
948 radiation data (illustrated in Figure 3), the misapplication of the VI-Ts method (explained in Figure 4),
949 and the uncertainties in daily net radiation (depicted in Figure 5). Designed to amalgamate bare soil and
950 full vegetation coverage, as ~~depicted~~ shown in Equation 1, the VISEA model encounters difficulties in
951 accurately estimating ET at higher latitudes, especially in conditions of reduced solar radiation. These
952 challenges are predominantly linked to the uncertainties associated with ERA5-Land shortwave radiation
953 data, further compounded by increased cloudiness levels in these regions, as highlighted by Babar et al.
954 (2019). Such uncertainties ~~have a substantial~~ substantially impact ~~on~~ the model's performance at higher
955 latitudes, affecting its reliability in these conditions. ~~Nevertheless, VISEA's ET estimates compare~~
956 ~~favorably with other ET data products in cold regions above 60°N, as indicated by the latitude zonal mean~~
957 ~~comparison in Figure 8.~~

958 ~~Despite these challenges, our analysis confirms the VISEA model's ability to provide valuable ET~~
959 ~~estimates during the growing season, evidenced by a high Nash-Sutcliffe efficiency (NSE) of 0.4 and a~~
960 ~~correlation coefficient (R) of 0.9 when compared against local measurements. These findings support the~~
961 ~~model's applicability for ET estimation in the 60°N to 90°N latitude range, highlighting its effectiveness~~
962 ~~and relevance during the vegetative growth period.~~

963 ~~We recognize that variations in the temporal coverage of ET products can introduce variability into~~
964 ~~our comparisons. To mitigate this, we have deliberately chosen validation datasets spanning from 2001~~
965 ~~to 2020, achieving a uniform analysis timeframe. This selection enabled us to utilize a diverse range of~~
966 ~~ET products, effectively minimizing the influence of temporal discrepancies on our comparative analysis.~~
967 ~~Concentrating on this two-decade interval has allowed us to robustly evaluate spatial and inter-annual ET~~
968 ~~variability, significantly reducing potential biases associated with differing dataset durations. This~~
969 ~~method enhances the clarity of our validation approach, solidifies the reliability of our comparisons, and~~
970 ~~ensures our analysis accurately reflects long-term ET dynamics.~~

971 ~~The VISEA ET product provides near real-time global evapotranspiration (ET) data with a mere one-~~
972 ~~week delay and a daily resolution of 0.05 degrees, making it a valuable asset for the research community.~~
973 ~~It empowers researchers by providing access to information on land surface water consumption in near-~~
974 ~~real time, which is crucial for monitoring and predicting droughts, and enables decision-makers to make~~
975 ~~well-informed choices. This not only enhances research efficiency but also supports more effective and~~
976 ~~expedited actions within the scientific and environmental research community.~~

977 The accuracy of the VISEA model could be enhanced by incorporating additional satellite and
978 climate data with higher resolution and improved accuracy. Moreover, the delay in providing ET data
979 could be reduced to three days or less by integrating real-time updated satellite and climate data. ~~In~~
980 ~~response to the suggestion to conclude our discussion with specific recommendations for future research~~
981 ~~directions, we recognize the importance of addressing the identified gaps and uncertainties.~~ We propose
982 ~~exploring the development of~~ developing alternative methods for estimating air temperature and net
983 radiation to ~~provide more accurate and reliable models~~ enhance accuracy. Additionally, incorporating
984 variables such as soil moisture and water availability into the model could further refine its precision. ~~By~~
985 ~~integrating these suggestions, we aim to outline~~ These improvements provide a comprehensive roadmap
986 ~~for future research that builds upon our findings, aiming to significantly contributing to the enhancement~~
987 ~~of environmental modelling and prediction within the field~~ enhance satellite-based near-real-time ET
988 modeling.

带格式的: 缩进: 首行缩进: 2 字符

设置了格式: 英语(美国)

设置了格式: 英语(美国)

设置了格式: 英语(美国)

设置了格式: 英语(美国)

989 6. Conclusion

990 ~~In recent decades, several~~ Several satellite-based ET products ~~using satellites~~ have been developed,
991 but few ~~of them estimate near-real-time global terrestrial evapotranspiration (ET). We have developed~~
992 VISEA ET, which only uses satellite-based input data and can provide near-real-time global terrestrial
993 ET estimates. Despite being updated at the fastest rate, the MOD16 ET dataset still encounters a delay of
994 more than two weeks. In this study, we provide a satellite-based near-real-time global daily terrestrial ET
995 estimates by incorporating near-real-time updated hourly shortwave radiation data from ERA5 and
996 MODIS land products at a 0.05° spatial resolution of 0.05°. The ~~assessments indicate that near-real-~~
997 ~~time ET estimation with VISEA achieves~~ accuracy of VISEA ET estimates is comparable accuracy to
998 ~~other existing data-ET products sooner than existing products and offers a significantly shorter time frame~~
999 ~~for daily data availability.~~

1000 ~~The new.~~ Our evaluations show that VISEA aligns well with measurements ~~at from~~ 149 globally
1001 distributed tower flux sites distributed globally in both daily and monthly time scales. It demonstrates
1002 competitive correlation coefficients and Nash-Sutcliffe efficiencies (NSEs) across most land cover types
1003 but exhibits higher biases. However, like the other five ET products, it encounters greater uncertainties
1004 for the SAV land cover type. In the comparison of the multiple-year average spatial distribution of other
1005 monthly ET products and ~~In addition, VISEA captures spatial patterns of evapotranspiration, aligning~~
1006 with GPCC precipitation, VISEA consistently demonstrates spatial patterns aligned with GPCC in most
1007 areas, featuring data across diverse geographical regions, particularly highlighting elevated values in
1008 tropical rainforest regions and lower values in arid and semi-arid zones. ~~This alignment underscores~~
1009 ~~VISEA's proficiency in portraying the spatial distribution of evapotranspiration, offering valuable~~
1010 ~~insights into water consumption dynamics across diverse geographical regions. However, VISEA~~
1011 ~~exhibits slightly higher~~ ET estimates are slightly too high in the Sahara region and lower and slightly too
1012 low in western Canada. Specifically, daily net radiation and ET estimations in the western Canada. ~~In~~
1013 ~~future studies, the VISA ET algorithm can be enhanced by incorporating more precise models for the~~
1014 ~~radiation estimation in savanna and the evaporation from the~~ of VISEA in Savannah and frozen surface.

带格式的: 缩进: 首行缩进: 2 字符

1015 ~~These surfaces need improvements will greatly contribute to enhancing the overall accuracy of the~~
1016 ~~algorithm. The satellite-based.~~ We plan to address these issues in future developments. The near-real-
1017 time global daily terrestrial ET estimates ~~could be beneficial provided by VISEA are valuable~~ for
1018 meteorology and hydrology applications ~~requiring real-time data~~, especially ~~in~~for coordinating relief
1019 efforts during droughts.

1020 7. Code Availability

1021 Python code to synthesise the results and to generate the figures of VISEA results and the codes for
1022 generating the global ET products can be obtained through the public repository at
1023 <https://doi.org/10.6084/m9.figshare.24647721.v1> (Huang, 2023c). [The VISEA code for calculating daily](#)
1024 [ET is written in C and can be executed on Windows 10 using an Intel\(R\) Core \(TM\) i7-8565U CPU @](#)
1025 [1.80GHz, 1.99 GHz, 16.0 GB RAM with Visual Studio 2019, or compatible platforms. Additionally, it](#)
1026 [can run on high-performance computing servers equipped with an Intel\(R\) Xeon\(R\) CPU E5-2680 in a](#)
1027 [CentOS environment. The system is scalable, supporting configurations ranging from 20 nodes and 656](#)
1028 [CPUs down to fewer nodes and CPUs as required.](#)

带格式的: 缩进: 首行缩进: 2 字符

设置了格式: 英语(美国)

1029 8. Data Availability

1030 ~~The VISEA ET data can be obtained from [https://data.tpdc.ac.cn/en/data/236e33bf-e66b-4682-bbc1-](https://data.tpdc.ac.cn/en/data/236e33bf-e66b-4682-bbc1-274de1debed3)~~
1031 ~~[274de1debed3](https://data.tpdc.ac.cn/en/data/236e33bf-e66b-4682-bbc1-274de1debed3) (Huang, 2023a).~~

1032 8. Data Availability

1033 [The VISEA ET data can be obtained from https://data.tpdc.ac.cn/en/data/236e33bf-e66b-4682-](https://data.tpdc.ac.cn/en/data/236e33bf-e66b-4682-bbc1-274de1debed3)
1034 [bbc1-274de1debed3](https://data.tpdc.ac.cn/en/data/236e33bf-e66b-4682-bbc1-274de1debed3) (Huang, 2023a). We are committed to continuously updating this dataset, ensuring
1035 [that the latest ET data will be consistently and promptly made available.](#)

1036 8.1 Input data

1037 MOD11C1 can be obtained at <https://e4ftl01.cr.usgs.gov/MOLT/MOD11C1.061/>. MOD09CMG
1038 can be obtained at <https://e4ftl01.cr.usgs.gov/MOLT/MOD09CMG.061/>. MCD43C3 can be obtained at
1039 <https://e4ftl01.cr.usgs.gov/MOTA/MCD43C3.061/>. MOD13C1 can be obtained at
1040 <https://e4ftl01.cr.usgs.gov/MOLT/MOD13C1.061/>. MCD12C1 can be obtained at
1041 <https://e4ftl01.cr.usgs.gov/MOLT/MOD21C1.061/>. ERA5-Land shortwave radiation data can be
1042 obtained at <https://cds.climate.copernicus.eu/cdsapp#!/dataset/reanalysis-era5-land?tab=form>.

带格式的: 缩进: 首行缩进: 2 字符

1043 8.2 Evaluation data

1044 FLUXNET2015 flux towers data (FLUXNET2015: CC-BY-4.0 33) can be obtained at
1045 <https://fluxnet.org/data/download-data/>. The GLEAM 3.8a ET dataset was obtained from
1046 <https://www.gleam.eu/#downloads> (an email is required to receive a password for the SFTP). The
1047 FLUXCOM ET dataset was freely available (CC4.0 BY licence) from <https://www.fluxcom.org/EF->

带格式的: 缩进: 首行缩进: 2 字符

1048 Download/ the Data Portal (an email is required to are receive a password for the FTP). MOD16 ET with
1049 the resolution of 0.05° was freely downloaded from
1050 http://files.ntsg.umt.edu/data/NTSG_Products/MOD16/MOD16A2_MONTHLY.MERRA_GMAO_1k
1051 [mALB/Previous/](http://files.ntsg.umt.edu/data/ET_global_monthly_ORIG/Global_1DegResolution/ASCIIFormat/). Additionally, the AVHRR ET dataset with 1° was sourced from
1052 http://files.ntsg.umt.edu/data/ET_global_monthly_ORIG/Global_1DegResolution/ASCIIFormat/.
1053 Lastly, the PML ET dataset was obtained from [https://www.tpsc.ac.cn/zh-hans/data/48c16a8d-d307-](https://www.tpsc.ac.cn/zh-hans/data/48c16a8d-d307-4973-abab-972e9449627c)
1054 [4973-abab 972e9449627c](https://www.tpsc.ac.cn/zh-hans/data/48c16a8d-d307-4973-abab-972e9449627c).

1055 The precipitation from Global Precipitation Climatology Centre (GPCC) data was as obtained at
1056 [https://cds.climate.copernicus.eu/cdsapp#!/dataset/insitu-gridded-observations-global-and-](https://cds.climate.copernicus.eu/cdsapp#!/dataset/insitu-gridded-observations-global-and-regional?tab=form)
1057 [regional?tab=form](https://cds.climate.copernicus.eu/cdsapp#!/dataset/insitu-gridded-observations-global-and-regional?tab=form). The precipitation from Global Unified Gauge-Based Analysis of Daily Precipitation
1058 (CPC) was obtained at https://downloads.psl.noaa.gov/Datasets/cpc_global_precip/precip.2022.nc

1059 Other data that supports the analysis and conclusions of this work is available at
1060 https://figshare.com/articles/dataset/Satellite-based_Near-Real
1061 [Time_Global_Daily_Terrestrial_Evapotranspiration_Estimates/24669306](https://figshare.com/articles/dataset/Satellite-based_Near-Real) ([Huang, — 2023d](#))([Huang,](#)
1062 [2023d](#)).
1063

1064 **Appendix**

1065 **Appendix A. Determining the vegetation fraction calculation:**

1066
$$f_{veg} = \frac{NDVI - NDVI_{min}}{NDVI_{max} - NDVI_{min}} \quad (A1)$$

1067 where the *NDVI* is the Normalized Difference Vegetation Index and can be calculated as:

1068
$$NDVI = \frac{R_{nir} - R_{red}}{R_{nir} + R_{red}} \quad (A2)$$

1069 where $NDVI_{min}$ is the *NDVI* of the bare soil without plants and $NDVI_{max}$ is the *NDVI* of the full
1070 vegetation cover, R_{nir} is the near-infrared reflectance and R_{red} is the red reflectance. The daily
1071 reflectance R_{nir} and R_{red} were measured by MODIS reflectance data MOD09CMG (Fig. 1). Based on
1072 Tang et al. (2009), we set $NDVI_{min} = 0.22$ and $NDVI_{max} = 0.83$. Missing observation for the daily
1073 MOD09CMG calculated *NDVI* data was filled with the 16-day averaged *NDVI* values in the
1074 MOD13Q1 data product (Fig. 1).

1075

1076 **Appendix B. Determining the instantaneous EF:**

1077 Combining Eq. 1 and 4, we first calculated the instantaneous evaporation fraction, EF^i as:

$$1078 \quad EF^i = f_{veg} \frac{Q_{veg}^i}{Q^i} EF_{veg}^i + (1 - f_{veg}) \frac{Q_{soil}^i}{Q^i} EF_{soil}^i \quad (B1)$$

1079 where the superscript i stands for the instantaneous value of the parameter, EF_{veg}^i and EF_{soil}^i are the
1080 instantaneous full vegetation coverage and bare soil EF, respectively. EF_{veg}^i can be expressed as a
1081 function of instantaneously parameters as (Nishida et al., 2003):

$$1082 \quad EF_{veg}^i = \frac{\alpha \Delta^i}{\Delta^i + \gamma(1 + r_{a,veg}^i / 2 + r_{a,veg}^i)} \quad (B2)$$

1083 where α is the Priestley-Taylor parameter, which was set to 1.26 for wet surfaces (De Bruin, 1983); Δ^i is
1084 the slope of the saturated vapor pressure, which is a function of the temperature (Pa K^{-1}); γ is the
1085 psychrometric constant (Pa K^{-1}); $r_{a,veg}^i$ is the instantaneous surface resistance of the vegetation canopy (s m^{-1}); $r_{a,veg}^i$
1086 is the instantaneous aerodynamics resistance of the vegetation canopy (s m^{-1}). EF_{soil}^i was
1087 expressed by Nishida et al. (2003) as a function of the instantaneous soil temperature and the available
1088 energy based on the energy budget of the bare soil:

$$1089 \quad EF_{soil}^i = \frac{T_{soil,max}^i - T_{soil}^i}{T_{soil,max}^i - T_a^i} \frac{Q_{soil}^i}{Q_{soil}^i} \quad (B3)$$

1090 where $T_{soil,max}^i$ is the instantaneous maximum possible temperature at the surface reached when the land
1091 surface is dry (K), T_{soil}^i is the instantaneous temperature of the bare soil (K), T_a^i is the instantaneous air
1092 temperature, Q_{soil}^i is the instantaneous available energy when T_{soil}^i is equal to T_a^i (W m^{-2}).

带格式的: 段落间距段后: 1 行

带格式的: 段落间距段后: 1 行

1094 **Appendix C. Determining of decoupling factor:**

1095 Ω_i^* is the value of the decoupling factor, Ω , for wet surface. According to Pereira (2004), Ω and Ω^*
1096 can be expressed as:

1097
1098

1099
$$\Omega = \frac{1}{1 + \frac{\gamma}{\Delta} r_c} \quad (\text{C4B1})$$

1100
$$\Omega^* = \frac{1}{1 + \frac{\gamma}{\Delta} r^*} \quad (\text{C2B2})$$

1101
$$r^* = \frac{(\Delta + \gamma) \rho C_p VPD}{\Delta \gamma (R_n - G)} \quad (\text{C3B3})$$

1102 where r_c is the surface resistance (s m^{-1}); r_a is the aerodynamic resistance (s m^{-1}); the calculation details
1103 of instantaneous and daily r_c and r_a for vegetation and soil are explained in Appendix A. r^* is the critical
1104 surface resistance when the actual evapotranspiration equals the potential evaporation (called equilibrium
1105 evapotranspiration, s m^{-1}); ρ is the air density (kg m^{-3}); C_p is the specific heat of the air ($\text{J kg}^{-1} \text{K}^{-1}$); VPD
1106 is the vapor pressure deficit of the air (Pa). Δ is the slope of the saturated vapor pressure (Pa K^{-1}).

1107

带格式的: 缩进: 首行缩进: 2 字符, 段落间距段后: 1 行

设置了格式: 字体: Cambria Math

设置了格式: 字体: Cambria Math

Appendix D. Determining the resistances of vegetation canopy and bare soil surface

The canopy surface resistance of the vegetation, denoted as $r_{c\ veg}$ ($s\ m^{-1}$), was determined using the relationship established by Jarvis et al. (1976), is equivalent to:

$$\frac{1}{r_{c\ veg}} = \frac{f_1(T_a)f_2(PAR)f_3(VPD)f_4(\varphi)f_5(CO_2)}{r_{c\ MIN}} + \frac{1}{r_{c\ cuticle}} \quad (D1C1)$$

The minimum resistance $r_{c\ MIN}$ ($s\ m^{-1}$) is defined as 33 ($s\ m^{-1}$) for cropland and 50 ($s\ m^{-1}$) for forest as determined by Tang et al. (2009); the canopy resistance related to diffusion through the cuticle layer of leaves $r_{c\ cuticle}$ is set at 100,000 ($s\ m^{-1}$) in the Biome-BGC model is according to White et al. (2000). The relationships involving air temperature T_a , $f_1(T_a)$ and photosynthetic active radiation PAR , $f_2(PAR)$ expressed by the functions provided Jarvis et al. (1976):

$$f_1(T_a) = \left(\frac{T_a - T_n}{T_o - T_n} \right) \left(\frac{T_x - T_a}{T_x - T_o} \right)^{\frac{T_x - T_a}{T_o - T_n}} \quad (D2C2)$$

The minimum, optimal, and maximum temperatures for stomatal activity are denoted as T_n , T_o and T_x , respectively. As per Tang et al. (2009), T_n is set to 275.85 K, T_o to 304.25 K, and T_x to 318.45 K. The expression for the function $f_2(PAR)$ is provided below:

$$f_2(PAR) = \frac{PAR}{PAR + A} \quad (D3C3)$$

where PAR is photosynthetic active radiation per unit area and time ($\mu\ mol\ m^{-2}\ s^{-1}$) calculated by incoming solar radiation multiplied by 2.05 (White et al., 2000); A is a parameter related to photon absorption efficiency at low light intensity, which was set to 152 $\mu\ mol\ m^{-2}\ s^{-1}$; Nishida³² found that in Eq. D1 the following functions can be omitted without great loss of accuracy: the functions depending on vapor pressure deficit, $f_3(VPD)$, leaf water potential $f_4(\varphi)$ and carbon dioxide vapor pressure, $f_5(CO_2)$.

The photosynthetic active radiation per unit area and time (PAR), measured in $\mu\ mol\ m^{-2}\ s^{-1}$, is computed by multiplying incoming solar radiation by 2.05, as outlined by White et al. (2000). The parameter A , associated with photon absorption efficiency at low light intensity, is established at 152 $\mu\ mol\ m^{-2}\ s^{-1}$. Nishida et al. (2003) observed that, in Eq. D1, the functions tied to vapor pressure deficit $f_3(VPD)$, leaf water potential $f_4(\varphi)$, and carbon dioxide vapor pressure $f_5(CO_2)$ can be omitted without significant loss of accuracy. Tang et al. (2009) employed this canopy resistance approach to estimate evapotranspiration (ET) at a 500-meter resolution in the Kalam river basin. The evaluation of their results indicated that the simplification of these calculations did not significantly impact the final accuracy of ET estimates. Additionally, Huang et al. (2017, 2021, and 2023) evaluated this method for 0.05-degree ET assessments across China. [The evaluation results also demonstrated. In this study, we follow the methodologies originally developed by Tang et al. \(2009\) and Nishida \(2003\), with the goal of enhancing the VISEA model to accurately estimate daily scale evaporation fraction and net radiation. These efforts](#)

1141 build on earlier work by Huang et al. (2017, 2021, and 2023) that the reduction in introduced vapor
 1142 pressure deficit (VPD) and leaf water potential had minimal effects on the final calculating canopy
 1143 resistance. However, comparative analyses between VISEA and other models, such as PML and
 1144 MOD16—particularly PML, which integrates VPD as a limiting factor in estimating GPP and ET
 1145 estimates—show that VISEA maintains accuracy without significant biases. It is important to note that
 1146 none of the ET models in our comparison directly incorporate leaf water potential into their canopy
 1147 resistance calculations. We are committed to addressing these gaps in our future studies.

设置了格式: 英语(美国)

设置了格式: 英语(美国)

设置了格式: 英语(美国)

设置了格式: 英语(美国)

1148 The aerodynamic resistance of the canopy, denoted as $r_{a\ veg}$ ($s\ m^{-1}$), is computed for forest cover,
 1149 grassland, and cropland using the empirical formulae presented by Nishida et al. (2003) for both
 1150 instantaneous and daily values.

$$1151 \quad \frac{1}{r_{a\ veg\ (forest)}} = 0.008U_{50m} \quad (D4C4)$$

1152 The wind speed at a height of 50 meters above the canopy (U_{50m}) is used to determine the
 1153 aerodynamic resistance for grassland and cropland, as follows:

$$1154 \quad \frac{1}{r_{a\ veg\ (grassland\ \&\ cropland)}} = 0.003U_{1m} \quad (D5C5)$$

1155 where U_{1m} is the wind speed 1m above the canopy ($m\ s^{-1}$). The wind speed as a function of the
 1156 height z , $U(z)$ can be calculated by the logarithm profile of wind. A recent study found that the velocity
 1157 log law does not apply to a stratified atmospheric boundary layer (Cheng et al., 2011). Thus D4 and D5
 1158 are valid under neutral boundary layer conditions. Since $r_{a\ veg}$ is calculated differently for forests (Eq.
 1159 D4) and grasslands/croplands (Eq. D5), we used the land cover classes from the yearly International
 1160 Geosphere-Biosphere Programme (IGBP) (MCD12C1) to identify the land cover and choice the different
 1161 equation of $r_{a\ veg}$. U_{50m} and U_{1m} were calculated by the logarithm profile of wind:

$$1162 \quad U(z) = U_{shear} \ln \left[\frac{(z-d)}{z_0} \right] / k \quad (D6C6)$$

1163 where U_{shear} is the shear velocity ($m\ s^{-1}$); z is the height (m); d is the surface displacement (m); z_0
 1164 is the roughness length, we followed Nishida et al. (2003), set as 0.005 m for bare soil and 0.01 m for
 1165 grassland; k is the von Kármán's constant and set as 0.4 following Nishida (Nishida et al., 2003). The
 1166 shear velocity U_{shear} was calculated as:

$$1167 \quad U_{shear} = U_{1m\ soil} \frac{0.4}{\ln \left(\frac{1}{0.005} \right)} \quad (D7C7)$$

1168 where the $U_{1m\ soil}$ is the wind speed of bare soil at 1 m height ($m\ s^{-1}$), it was calculated as:

$$1169 \quad U_{1m\ soil} = 1/0.0015 r_{a\ soil} \quad (D8C8)$$

1170 The Vegetation Index-surface Temperature (VI-T_s) diagram (Nishida et al., 2003) can be utilized to
 1171 compute the instantaneous air temperature. This is achieved by utilizing MODIS instantaneous surface
 1172 temperature/emissivity data (MOD11C1) and daily-calculated NDVI as input parameters.

1173 The aerodynamic resistance of the bare soil, denoted as $r_{a\ soil}$ ($s\ m^{-1}$), was determined by Nishida
 1174 et al. (2003). This calculation assumes that the maximum surface temperature of bare soil $T_{soil\ max}$ (K)
 1175 happens when the sum of latent heat flux and sensible heat flux of the bare soil, referred to as the available
 1176 energy of bare soil Q_{soil} ($W\ m^{-2}$), is utilized as the sensible heat flux, while the latent heat flux is set to
 1177 zero.

$$1178 \quad r_{a\ soil} = \frac{\rho C_p (T_{soil\ max} - T_a)}{Q_{soil}} \quad (D9C9)$$

1179 $r_{a\ soil}$ is the aerodynamic resistance of the bare soil, ($s\ m^{-1}$), ρ is the air density, $kg\ m^{-3}$; C_p is the
 1180 specific heat of the air, ($J\ kg^{-1}\ K^{-1}$); T_a is the air temperature (K), Q_{soil} is the available energy of bare soil
 1181 ($W\ m^{-2}$).

1182 To compute the canopy surface resistance of bare soil, denoted as $r_{c\ soil}$ ($s\ m^{-1}$), we adhere to the
 1183 methodologies outlined in the works of Griend and Owe (1994) and Mu et al. (2007):

$$1184 \quad r_{c\ soil} = r_{tot} - r_{a\ soil} \quad (D4C10)$$

$$1185 \quad r_{tot} = \frac{1.0}{\left(\frac{T_a}{293.15}\right)^{1.75} \frac{101300}{P}} * 107.0 \quad (D4C11)$$

1186 The total aerodynamic resistance r_{tot} ($s\ m^{-1}$) is composed of the aerodynamic resistance over the
 1187 bare soil $r_{a\ soil}$ ($s\ m^{-1}$), with atmospheric pressure P set at 101,300 Pa.

1188

1189 **Appendix E.D. The calculation of atmospheric emissivity for clear sky**

1190 As per Brutsaert (1975), the atmospheric emissivity ε_a^d for clear sky under standard humidity and
1191 temperature conditions is

1192
$$\varepsilon_a^d = 1.24 \times (e_a^d / T_a^d)^{1/7} \quad (\text{E4D1})$$

1193 where e_a^d represents the daily water vapor pressure (kPa). To calculate e_a^d , it is necessary to
1194 compute the slope of the saturated vapor (Δ) as:

1195
$$\Delta = \frac{4098 [0.6108 \exp(\frac{17.27T_a}{T_a+237.3})]}{(T_a+237.3)^2} \quad (\text{E2D2})$$

1196 VPD is the vapor pressure deficit of the air (kPa), which is expressed as:

1197
$$\text{VPD} = e^0(T_a) - e_a \quad (\text{E3D3})$$

1198
$$e^0(T_a) = 0.6108 \exp \left[\frac{17.27T_a}{T_a+237.3} \right] \quad (\text{E4D4})$$

1199
$$e_a = e^0(T_{dew}) \quad (\text{E5D5})$$

1200
$$e^0(T_{dew}) = 0.6108 \exp \left[\frac{17.27T_{dew}}{T_{dew}+237.3} \right] \quad (\text{E6D6})$$

1201 The expression within parentheses denotes the independent variable, where, $e^0(T_a)$ represents the
1202 saturation vapor pressure (kPa) at the air temperature T_a (°C); e_a is the actual vapor pressure (kPa);
1203 $e^0(T_{dew})$ is the saturation vapor pressure (kPa) at the dew point temperature T_{dew} (°C). For forest, water
1204 surface, and cropland T_{dew} is set to the minimum air temperature during the day. In arid regions such as
1205 bare soil and non-irrigated grassland, T_{dew} may be 2-3 °C lower than T_{min} . Therefore, 2 °C is subtracted
1206 is subtracted from T_{min} in arid and semiarid areas to derive T_{dew} . While these simplifications might
1207 introduce a bias in the final calculated ET value, our initial results indicate that the effect is negligible.

1208

1209 **Acknowledgements**

1210 This study is supported by the National Key Research and Development Program of China
1211 (No.2017YFA0603703). We employed ChatGPT3.5 to enhance the quality of our English writing and
1212 grammar.

带格式的: 缩进: 首行缩进: 2 字符

1213 **Author contributions**

1214 L. H. had the original idea and drafted the paper with help from Y. L.; J. M. C. Q. T., T. S., W. C.
1215 and W. S. participated in the discussion and the many manuscript revisions.

带格式的: 缩进: 首行缩进: 2 字符

1216 **Competing interests**

1217 The authors declare no competing interests.

带格式的: 缩进: 首行缩进: 2 字符

1218 **References**

1219 [Albergel, C., Balsamo, G., de Rosnay, P., Muñoz-Sabater, J., and Boussetta, S.: A bare ground](#)
1220 [evaporation revision in the ECMWF land-surface scheme: evaluation of its impact using ground soil](#)
1221 [moisture and satellite microwave data, *Hydrology and Earth System Sciences*, 16, 3607–3620,](#)
1222 <https://doi.org/10.5194/hess-16-3607-2012>, 2012.

1223 [Anderson, M. C., Yang, Y., Xue, J., Knipper, K. R., Yang, Y., Gao, F., Hain, C. R., Kustas, W. P.,](#)
1224 [Cawse-Nicholson, K., Hulley, G., Fisher, J. B., Alfieri, J. G., Meyers, T. P., Prueger, J., Baldocchi,](#)
1225 [D. D., and Rev-Sanchez, C.: Interoperability of ECOSTRESS and Landsat for mapping](#)
1226 [evapotranspiration time series at sub-field scales, *Remote Sensing of Environment*, 252, 112189,](#)
1227 <https://doi.org/10.1016/j.rse.2020.112189>, 2021.

1228 Aschonitis, V., Touloumidis, D., ten Veldhuis, M.-C., and Coenders-Gerrits, M.: Correcting
1229 Thornthwaite potential evapotranspiration using a global grid of local coefficients to support
1230 temperature-based estimations of reference evapotranspiration and aridity indices, *Earth System*
1231 *Science Data*, 14, 163–177, <https://doi.org/10.5194/essd-14-163-2022>, 2022.

1232 Awada, H., Di Prima, S., Sirca, C., Giadrossich, F., Marras, S., Spano, D., and Pirastru, M.: A remote
1233 sensing and modeling integrated approach for constructing continuous time series of daily actual
1234 evapotranspiration, *Agricultural Water Management*, 260, 107320,
1235 <https://doi.org/10.1016/j.agwat.2021.107320>, 2022.

1236 Babar, B., Graversen, R., and Boström, T.: Solar radiation estimation at high latitudes: Assessment
1237 of the CMSAF databases, ASR and ERA5, *Solar Energy*, 182, 397–411,
1238 <https://doi.org/10.1016/j.solener.2019.02.058>, 2019.

1239 Baldocchi, D., Falge, E., Gu, L., Olson, R., Hollinger, D., Running, S., Anthoni, P., Bernhofer, C.,
1240 Davis, K., Evans, R., Fuentes, J., Goldstein, A., Katul, G., Law, B., Lee, X., Malhi, Y., Meyers, T.,
1241 Munger, W., Oechel, W., U, K. T. P., Pilegaard, K., Schmid, H. P., Valentini, R., Verma, S., Vesala,
1242 T., Wilson, K., and Wofsy, S.: FLUXNET: A New Tool to Study the Temporal and Spatial Variability
1243 of Ecosystem-Scale Carbon Dioxide, Water Vapor, and Energy Flux Densities, *Bulletin of the*
1244 *American Meteorological Society*, 82, 2415–2434, [https://doi.org/10.1175/1520-0477\(2001\)082<2415:FANTTS>2.3.CO;2](https://doi.org/10.1175/1520-0477(2001)082<2415:FANTTS>2.3.CO;2), 2001.

1246 Barrios, J. M., Ghilain, N., Arboleda, A., and Gellens-Meulenberghs, F.: Retrieving daily
1247 evapotranspiration from the combination of geostationary and polar-orbit satellite data, in: 2015 8th
1248 International Workshop on the Analysis of Multitemporal Remote Sensing Images (Multi-Temp),
1249 2015 8th International Workshop on the Analysis of Multitemporal Remote Sensing Images (Multi-

1250 Temp), 1–4, <https://doi.org/10.1109/Multi-Temp.2015.7245797>, 2015.

1251 Becker, A., Finger, P., Meyer-Christoffer, A., Rudolf, B., Schamm, K., Schneider, U., and Ziese, M.:
 1252 A description of the global land-surface precipitation data products of the Global Precipitation
 1253 Climatology Centre with sample applications including centennial (trend) analysis from 1901–
 1254 present, *Earth System Science Data*, 5, 71–99, <https://doi.org/10.5194/essd-5-71-2013>, 2013.

1255 Brutsaert, W.: On a derivable formula for long-wave radiation from clear skies, *Water Resources
 1256 Research*, 11, 742–744, <https://doi.org/10.1029/WR011i005p00742>, 1975.

1257 Chang, K. and Zhang, Q.: Modeling of downward longwave radiation and radiative cooling potential
 1258 in China, *Journal of Renewable and Sustainable Energy*, 11, 066501,
 1259 <https://doi.org/10.1063/1.5117319>, 2019.

1260 Chen, X., Su, Z., Ma, Y., Trigo, I., and Gentile, P.: Remote Sensing of Global Daily
 1261 Evapotranspiration based on a Surface Energy Balance Method and Reanalysis Data, *Journal of
 1262 Geophysical Research: Atmospheres*, 126, e2020JD032873, <https://doi.org/10.1029/2020JD032873>,
 1263 2021.

1264 Cheng, L., Xu, Z., Wang, D., and Cai, X.: Assessing interannual variability of evapotranspiration at
 1265 the catchment scale using satellite-based evapotranspiration data sets, *Water Resources Research*,
 1266 47, <https://doi.org/10.1029/2011WR010636>, 2011.

1267 Copernicus Climate Change Service: Crop productivity and evapotranspiration indicators from 2000
 1268 to present derived from satellite observations, <https://doi.org/10.24381/CDS.B2F6F9F6>, 2020.

1269 Cui, Y., Jia, L., and Fan, W.: Estimation of actual evapotranspiration and its components in an
 1270 irrigated area by integrating the Shuttleworth-Wallace and surface temperature-vegetation index
 1271 schemes using the particle swarm optimization algorithm, *Agricultural and Forest Meteorology*, 307,
 1272 108488, <https://doi.org/10.1016/j.agrformet.2021.108488>, 2021.

1273 De Bruin, H. a. R.: A Model for the Priestley-Taylor Parameter α , *J. Climate Appl. Meteor.*, 22, 572–
 1274 578, [https://doi.org/10.1175/1520-0450\(1983\)022<0572:AMFTPT>2.0.CO;2](https://doi.org/10.1175/1520-0450(1983)022<0572:AMFTPT>2.0.CO;2), 1983.

1275 [Didan, K.: MOD13C1 MODIS/Terra Vegetation Indices 16-Day L3 Global 0.05Deg CMG V006](https://doi.org/10.5067/MODIS/MOD13C1.006)
 1276 [\[Data set\], https://doi.org/10.5067/MODIS/MOD13C1.006, n.d.](https://doi.org/10.5067/MODIS/MOD13C1.006)

1277 [Fisher, J. B., Lee, B., Purdy, A. J., Halverson, G., Cawse-Nicholson, K., Wang, A., Anderson, R. G.,
 1278 Aragon, B., Arain, M. A., Baldocchi, D. D., Baker, J. M., Barral, H., Bernacchi, C., Bernhofer, C.,
 1279 Biraud, S., Bohrer, G., Brunsell, N. A., Cappelare, B., Castro-Contreras, S., Chun, J., Conrad, B.,
 1280 Cremonese, E., Demarty, J., Desai, A. R., De Ligne, A., Foltynová, L., Goulden, M., Griffis, T. J.,
 1281 Grünwald, T., Johnson, M. S., Kang, M., Kelbe, D., Kowalska, N., Lim, J. H., Mainassara, I., Lim,
 1282 J., McCabe, M., Missik, J., Mohanty, B., Moore, C., Morillas, L., Morrison, R., Munger, W., Posse,
 1283 G., Richardson, A. D., Russell, E., Ryu, Y., Sanchez-Azofeifa, G. A., Schmidt, M., Schwartz, E.,
 1284 Sharp, I., Šigut, L., Tang, Y., Lee, C. M., Hulley, G. C., Anderson, M., Hain, C., French, A. N., Wood,
 1285 E. F., and Hook, S. J.: First evapotranspiration results from NASA's ECOSTRESS mission, 2019,
 1286 H22B-07, 2019.](https://doi.org/10.5067/MODIS/MOD13C1.006)

1287 Fisher, J. B., Lee, B., Purdy, A. J., Halverson, G. H., Dohlen, M. B., Cawse-Nicholson, K., Wang,
 1288 A., Anderson, R. G., Aragon, B., Arain, M. A., Baldocchi, D. D., Baker, J. M., Barral, H., Bernacchi,
 1289 C. J., Bernhofer, C., Biraud, S. C., Bohrer, G., Brunsell, N., Cappelare, B., Castro-Contreras, S.,
 1290 Chun, J., Conrad, B. J., Cremonese, E., Demarty, J., Desai, A. R., De Ligne, A., Foltynová, L.,
 1291 Goulden, M. L., Griffis, T. J., Grünwald, T., Johnson, M. S., Kang, M., Kelbe, D., Kowalska, N.,
 1292 Lim, J.-H., Mainassara, I., McCabe, M. F., Missik, J. E. C., Mohanty, B. P., Moore, C. E., Morillas,
 1293 L., Morrison, R., Munger, J. W., Posse, G., Richardson, A. D., Russell, E. S., Ryu, Y., Sanchez-
 1294 Azofeifa, A., Schmidt, M., Schwartz, E., Sharp, I., Šigut, L., Tang, Y., Hulley, G., Anderson, M.,
 1295 Hain, C., French, A., Wood, E., and Hook, S.: ECOSTRESS: NASA's Next Generation Mission to
 1296 Measure Evapotranspiration From the International Space Station, *Water Resources Research*, 56,

- 1297 e2019WR026058, <https://doi.org/10.1029/2019WR026058>, 2020.
- 1298 [Friedl, M., D. Sulla Menashe.: MCD12C1 MODIS/Terra+Aqua Land Cover Type Yearly L3 Global
1299 0.05Deg CMG V006 \[Data set\]., https://doi.org/10.5067/MODIS/MCD12C1.006, 2015.](https://doi.org/10.5067/MODIS/MCD12C1.006)
- 1300 Fritschen, L. J. and Gay, L. W.: Soil Heat Flux, in: Environmental Instrumentation, edited by:
1301 Fritschen, L. J. and Gay, L. W., Springer, New York, NY, 86–92, [https://doi.org/10.1007/978-1-4612-
1302 6205-3_4](https://doi.org/10.1007/978-1-4612-6205-3_4), 1979.
- 1303 Goforth, M. A., Gilchrist, G. W., and Sirianni, J. D.: Cloud effects on thermal downwelling sky
1304 radiance, in: Thermosense XXIV, 203–213, <https://doi.org/10.1117/12.459570>, 2002.
- 1305 Griend, A. A. van de and Owe, M.: Bare soil surface resistance to evaporation by vapor diffusion
1306 under semiarid conditions, Water Resources Research, 30, 181–188,
1307 <https://doi.org/10.1029/93WR02747>, 1994.
- 1308 Halverson, G. H., Fisher, J., Jewell, L. A., Moore, G., Verma, M., McDonald, T., Kim, S., and Muniz,
1309 A.: Near Real-Time Monitoring of Global Evapotranspiration and its Application to Water Resource
1310 Management, 2016, H54D-01, 2016.
- 1311 Han, C., Ma, Y., Wang, B., Zhong, L., Ma, W., Chen, X., and Su, Z.: Long-term variations in actual
1312 evapotranspiration over the Tibetan Plateau, Earth System Science Data, 13, 3513–3524,
1313 <https://doi.org/10.5194/essd-13-3513-2021>, 2021.
- 1314 He, S., Zhang, Y., Ma, N., Tian, J., Kong, D., and Liu, C.: A daily and 500&thinspm coupled
1315 evapotranspiration and gross primary production product across China during 2000–2020, Earth
1316 System Science Data, 14, 5463–5488, <https://doi.org/10.5194/essd-14-5463-2022>, 2022.
- 1317 Huang, L.: Satellite-based Near-Real-Time Global Terrestrial Evapotranspiration Estimation Dataset,
1318 <https://doi.org/https://doi.org/10.11888/Terre.tpdc.300782>
1319 <https://cstr.cn/18406.11.Terre.tpdc.300782> ., 2023.
- 1320 Huang, L., Li, Z., Tang, Q., Zhang, X., Liu, X., and Cui, H.: Evaluation of satellite-based
1321 evapotranspiration estimates in China, JARS, 11, 026019, <https://doi.org/10.1117/1.JRS.11.026019>,
1322 2017.
- 1323 Huang, L., Steenhuis, T. S., Luo, Y., Tang, Q., Tang, R., Zheng, J., Shi, W., and Qiao, C.: Revisiting
1324 Daily MODIS Evapotranspiration Algorithm Using Flux Tower Measurements in China, Earth and
1325 Space Science, 8, e2021EA001818, <https://doi.org/10.1029/2021EA001818>, 2021.
- 1326 Huang, L., Luo, Y., Steenhuis, T., Tang, Q., Cheng, W., Shi, W., Xia, X., Zhao, D., and Liao, Z.: An
1327 Improved Satellite-Based Evapotranspiration Procedure for China, Earth and Space Science, 10,
1328 e2023EA002949, <https://doi.org/10.1029/2023EA002949>, 2023.
- 1329 Idso, S. B., Aase, J. K., and Jackson, R. D.: Net radiation — soil heat flux relations as influenced by
1330 soil water content variations, Boundary-Layer Meteorol, 9, 113–122,
1331 <https://doi.org/10.1007/BF00232257>, 1975.
- 1332 [Jaafar, H., Mourad, R., and Schull, M.: A global 30-m ET model \(HSEB\) using harmonized Landsat
1333 and Sentinel-2, MODIS and VIIRS: Comparison to ECOSTRESS ET and LST, Remote Sensing of
1334 Environment, 274, 112995, https://doi.org/10.1016/j.rse.2022.112995, 2022.](https://doi.org/10.1016/j.rse.2022.112995)
- 1335 [Jarlan, L., Balsamo, G., Lafont, S., Beljaars, A., Calvet, J. C., and Mougin, E.: Analysis of leaf area
1336 index in the ECMWF land surface model and impact on latent heat and carbon fluxes: Application
1337 to West Africa, Journal of Geophysical Research: Atmospheres, 113,
1338 https://doi.org/10.1029/2007JD009370, 2008.](https://doi.org/10.1029/2007JD009370)
- 1339 Jarvis, P. G., Monteith, J. L., and Weatherley, P. E.: The interpretation of the variations in leaf water

1340 potential and stomatal conductance found in canopies in the field, *Philosophical Transactions of the*
1341 *Royal Society of London. B, Biological Sciences*, 273, 593–610,
1342 <https://doi.org/10.1098/rstb.1976.0035>, 1976.

1343 Jiang, H., Yang, Y., Bai, Y., and Wang, H.: Evaluation of the Total, Direct, and Diffuse Solar
1344 Radiations From the ERA5 Reanalysis Data in China, *IEEE Geoscience and Remote Sensing Letters*,
1345 17, 47–51, <https://doi.org/10.1109/LGRS.2019.2916410>, 2020.

1346 Jung, M.: FLUXCOM Global Land Energy Fluxes,
1347 https://doi.org/10.17871/FLUXCOM_EnergyFluxes_v1, 2018.

1348 Jung, M., Reichstein, M., and Bondeau, A.: Towards global empirical upscaling of FLUXNET eddy
1349 covariance observations: validation of a model tree ensemble approach using a biosphere model,
1350 *Biogeosciences*, 6, 2001–2013, <https://doi.org/10.5194/bg-6-2001-2009>, 2009.

1351 Jung, M., Reichstein, M., Ciais, P., Seneviratne, S. I., Sheffield, J., Goulden, M. L., Bonan, G.,
1352 Cescatti, A., Chen, J., de Jeu, R., Dolman, A. J., Eugster, W., Gerten, D., Gianelle, D., Gobron, N.,
1353 Heinke, J., Kimball, J., Law, B. E., Montagnani, L., Mu, Q., Mueller, B., Oleson, K., Papale, D.,
1354 Richardson, A. D., Rouspard, O., Running, S., Tomelleri, E., Viovy, N., Weber, U., Williams, C.,
1355 Wood, E., Zaehle, S., and Zhang, K.: Recent decline in the global land evapotranspiration trend due
1356 to limited moisture supply, *Nature*, 467, 951–954, <https://doi.org/10.1038/nature09396>, 2010.

1357 Jung, M., Koirala, S., Weber, U., Ichii, K., Gans, F., Camps-Valls, G., Papale, D., Schwalm, C.,
1358 Tramontana, G., and Reichstein, M.: The FLUXCOM ensemble of global land-atmosphere energy
1359 fluxes, *Sci Data*, 6, 1–14, <https://doi.org/10.1038/s41597-019-0076-8>, 2019.

1360 Kondo Junsei: *Atmospheric Science near the Ground Surface*, University of Tokyo Press, Tokyo,
1361 324 pp., 2000.

1362 [Liu, Z., Jiang, L., Shi, C., Zhang, T., Zhou, Z., Liao, J., Yao, S., Liu, J., Wang, M., Wang, H., Liang,](#)
1363 [X., Zhang, Z., Yao, Y., Zhu, T., Chen, Z., Xu, W., Cao, L., Jiang, H., and Hu, K.: CRA-](#)
1364 [40/Atmosphere—The First-Generation Chinese Atmospheric Reanalysis \(1979–2018\): System](#)
1365 [Description and Performance Evaluation, *J Meteorol Res*, 37, 1–19, https://doi.org/10.1007/s13351-](#)
1366 [023-2086-x, 2023.](#)

1367 Martens, B., Miralles, D. G., Lievens, H., van der Schalie, R., de Jeu, R. A. M., Fernández-Prieto,
1368 D., Beck, H. E., Dorigo, W. A., and Verhoest, N. E. C.: GLEAM v3: satellite-based land evaporation
1369 and root-zone soil moisture, *Geoscientific Model Development*, 10, 1903–1925,
1370 <https://doi.org/10.5194/gmd-10-1903-2017>, 2017.

1371 Martens, B., Schumacher, D. L., Wouters, H., Muñoz-Sabater, J., Verhoest, N. E. C., and Miralles,
1372 D. G.: Evaluating the land-surface energy partitioning in ERA5, *Geoscientific Model Development*,
1373 13, 4159–4181, <https://doi.org/10.5194/gmd-13-4159-2020>, 2020.

1374 Martin Jung, Sujan Koirala, Ulrich Weber, Kazuhito Ichii, Fabian Gans, Gustau Camps-Valls, Dario
1375 Papale, Christopher Schwalm, Gianluca tramontana & Markus Reichstein: FLUXCOM Global Land
1376 Energy Fluxes, https://doi.org/10.17871/FLUXCOM_EnergyFluxes_v1, 2018.

1377 [Miller, M. J., Beljaars, A. C. M., and Palmer, T. N.: The Sensitivity of the ECMWF Model to the](#)
1378 [Parameterization of Evaporation from the Tropical Oceans, *Journal of Climate*, 5, 418–434,](#)
1379 [https://doi.org/10.1175/1520-0442\(1992\)005<0418:TSOTEM>2.0.CO;2, 1992.](#)

1380 Miralles, D. G., Holmes, T. R. H., De Jeu, R. a. M., Gash, J. H., Meesters, A. G. C. A., and Dolman,
1381 A. J.: Global land-surface evaporation estimated from satellite-based observations, *Hydrology and*
1382 *Earth System Sciences*, 15, 453–469, <https://doi.org/10.5194/hess-15-453-2011>, 2011.

1383 Mu, Q., Heinsch, F. A., Zhao, M., and Running, S. W.: Development of a global evapotranspiration
1384 algorithm based on MODIS and global meteorology data, *Remote Sensing of Environment*, 111,

- 1385 519–536, <https://doi.org/10.1016/j.rse.2007.04.015>, 2007.
- 1386 Mu, Q., Zhao, M., and Running, S. W.: Improvements to a MODIS global terrestrial
1387 evapotranspiration algorithm, *Remote Sensing of Environment*, 115, 1781–1800,
1388 <https://doi.org/10.1016/j.rse.2011.02.019>, 2011.
- 1389 [Mu, Q., Zhao, M., Kimball, J. S., McDowell, N. G., and Running, S. W.: A Remotely Sensed Global
1390 Terrestrial Drought Severity Index, *Bulletin of the American Meteorological Society*, 94, 83–98,
1391 <https://doi.org/10.1175/BAMS-D-11-00213.1>, 2013.](https://doi.org/10.1175/BAMS-D-11-00213.1)
- 1392 Muñoz Sabater, J.: ERA5-Land hourly data from 1950 to present., [https://doi.org/DOI:
1393 10.24381/cds.e2161bac](https://doi.org/DOI:10.24381/cds.e2161bac), 2019.
- 1394 Naud, C. M., Booth, J. F., and Genio, A. D. D.: Evaluation of ERA-Interim and MERRA Cloudiness
1395 in the Southern Ocean, *Journal of Climate*, 27, 2109–2124, [https://doi.org/10.1175/JCLI-D-13-
00432.1](https://doi.org/10.1175/JCLI-D-13-
1396 00432.1), 2014.
- 1397 Nishida, K., Nemani, R. R., Running, S. W., and Glassy, J. M.: An operational remote sensing
1398 algorithm of land surface evaporation, *Journal of Geophysical Research: Atmospheres*, 108,
1399 <https://doi.org/10.1029/2002JD002062>, 2003.
- 1400 Panagos, P., Borrelli, P., Meusburger, K., Yu, B., Klik, A., Yang, J., Ni, J., Chattopadhyay, N.,
1401 Sadeghi, S. H., Hazbavi, Z., Zabihi, M., Larionov, G., Krasnov, S., Gorobets, A., Levi, Y., Erpul, G.,
1402 Birkel, C., and Ballabio, C.: Global rainfall erosivity assessment based on high-temporal resolution
1403 rainfall records, *Scientific Reports*, 7, <https://doi.org/10.1038/s41598-017-04282-8>, 2017.
- 1404 Pastorello, G., Trotta, C., Canfora, E., Chu, H., Christianson, D., Cheah, Y.-W., Poindexter, C., Chen,
1405 J., Elbashandy, A., Humphrey, M., Isaac, P., Polidori, D., Reichstein, M., Ribeca, A., van Ingen, C.,
1406 Vuichard, N., Zhang, L., Amiro, B., Ammann, C., Arain, M. A., Ardö, J., Arkebauer, T., Arndt, S. K.,
1407 Arriga, N., Aubinet, M., Aurela, M., Baldocchi, D., Barr, A., Beamesderfer, E., Marchesini, L. B.,
1408 Bergeron, O., Beringer, J., Bernhofer, C., Berveiller, D., Billesbach, D., Black, T. A., Blanken, P. D.,
1409 Bohrer, G., Boike, J., Bolstad, P. V., Bonal, D., Bonnefond, J.-M., Bowling, D. R., Bracho, R.,
1410 Brodeur, J., Brümmer, C., Buchmann, N., Burban, B., Burns, S. P., Buysse, P., Cale, P., Cavagna,
1411 M., Cellier, P., Chen, S., Chini, I., Christensen, T. R., Cleverly, J., Collalti, A., Consalvo, C., Cook,
1412 B. D., Cook, D., Coursolle, C., Cremonese, E., Curtis, P. S., D’Andrea, E., da Rocha, H., Dai, X.,
1413 Davis, K. J., Cinti, B. D., Grandcourt, A. de, Ligne, A. D., De Oliveira, R. C., Delpierre, N., Desai,
1414 A. R., Di Bella, C. M., Tommasi, P. di, Dolman, H., Domingo, F., Dong, G., Dore, S., Duce, P.,
1415 Dufrene, E., Dunn, A., Dušek, J., Eamus, D., Eichelmann, U., ElKhidir, H. A. M., Eugster, W.,
1416 Ewenz, C. M., Ewers, B., Famulari, D., Fares, S., Feigenwinter, I., Feitz, A., Fensholt, R., Filippa,
1417 G., Fischer, M., Frank, J., Galvagno, M., et al.: The FLUXNET2015 dataset and the ONEFlux
1418 processing pipeline for eddy covariance data, *Sci Data*, 7, 225, [https://doi.org/10.1038/s41597-020-
0534-3](https://doi.org/10.1038/s41597-020-
1419 0534-3), 2020.
- 1420 Pereira, A. R.: The Priestley–Taylor parameter and the decoupling factor for estimating reference
1421 evapotranspiration, *Agricultural and Forest Meteorology*, 125, 305–313,
1422 <https://doi.org/10.1016/j.agrformet.2004.04.002>, 2004.
- 1423 [Schaaf, C., Wang, Z.: MCD43C1 MODIS/Terra+Aqua BRDF/Albedo Model Parameters Daily L3
1424 Global 0.05Deg CMG V006 \[Data set\], <https://doi.org/10.5067/MODIS/MCD43C1.006>, 2015.](https://doi.org/10.5067/MODIS/MCD43C1.006)
- 1425 Schneider, U., Becker, A., Finger, P., Meyer-Christoffer, A., Ziese, M., and Rudolf, B.: GPCP’s new
1426 land surface precipitation climatology based on quality-controlled in situ data and its role in
1427 quantifying the global water cycle, *Theor Appl Climatol*, 115, 15–40,
1428 <https://doi.org/10.1007/s00704-013-0860-x>, 2014.
- 1429 Schneider, U., Finger, P., Meyer-Christoffer, A., Rustemeier, E., Ziese, M., and Becker, A.:
1430 Evaluating the Hydrological Cycle over Land Using the Newly-Corrected Precipitation Climatology
1431 from the Global Precipitation Climatology Centre (GPCC), *Atmosphere*, 8, 52,

- 1432 <https://doi.org/10.3390/atmos8030052>, 2017.
- 1433 Su, B., Huang, J., Mondal, S. K., Zhai, J., Wang, Y., Wen, S., Gao, M., Lv, Y., Jiang, S., Jiang, T.,
1434 and Li, A.: Insight from CMIP6 SSP-RCP scenarios for future drought characteristics in China,
1435 *Atmospheric Research*, 105375, <https://doi.org/10.1016/j.atmosres.2020.105375>, 2020.
- 1436 Sun, S., Bi, Z., Xiao, J., Liu, Y., Sun, G., Ju, W., Liu, C., Mu, M., Li, J., Zhou, Y., Li, X., Liu, Y., and
1437 Chen, H.: A global 5 km monthly potential evapotranspiration dataset (1982–2015) estimated
1438 by the Shuttleworth-Wallace model, *Earth System Science Data Discussions*, 1–45,
1439 <https://doi.org/10.5194/essd-2023-38>, 2023.
- 1440 Tang, Q., Peterson, S., Cuenca, R. H., Hagimoto, Y., and Lettenmaier, D. P.: Satellite-based near-
1441 real-time estimation of irrigated crop water consumption, *Journal of Geophysical Research: Journal of Geophysical Research: Atmospheres*, 114, <https://doi.org/10.1029/2008JD010854>, 2009.
- 1443 Tang, R. and Li, Z.-L.: An improved constant evaporative fraction method for estimating daily
1444 evapotranspiration from remotely sensed instantaneous observations, *Geophysical Research Letters*,
1445 44, 2319–2326, <https://doi.org/10.1002/2017GL072621>, 2017.
- 1446 Tang, R., Li, Z.-L., Sun, X., and Bi, Y.: Temporal upscaling of instantaneous evapotranspiration on
1447 clear-sky days using the constant reference evaporative fraction method with fixed or variable
1448 surface resistances at two cropland sites, *Journal of Geophysical Research: Atmospheres*, 122, 784–
1449 801, <https://doi.org/10.1002/2016JD025975>, 2017.
- 1450 Taylor, K. E.: Summarizing multiple aspects of model performance in a single diagram, *Journal of*
1451 *Geophysical Research: Atmospheres*, 106, 7183–7192, <https://doi.org/10.1029/2000JD900719>,
1452 2001.
- 1453 Udo; Becker, Andreas; Finger, Peter; Meyer-Christoffer, Anja; Rudolf, Bruno; Ziese, Markus: GPCP
1454 Full Data Reanalysis Version 6.0 at 2.5°: Monthly Land-Surface Precipitation from Rain-Gauges
1455 built on GTS-based and Historic Data., https://doi.org/DOI:10.5676/DWD_GPCC/FD_M_V7_250,
1456 2011.
- 1457 [Vermote, E.: MOD09CMG MODIS/Terra Surface Reflectance Daily L3 Global 0.05Deg CMG V006](https://doi.org/10.5067/MODIS/MOD09CMG.006)
1458 [\[Data set\], https://doi.org/10.5067/MODIS/MOD09CMG.006, 2015.](https://doi.org/10.5067/MODIS/MOD09CMG.006)
- 1459 [Wan, Z., Hook, S., Hulley, G.: MOD11C1 MODIS/Terra Land Surface Temperature/Emissivity Daily](https://doi.org/10.5067/MODIS/MOD11C1.006)
1460 [L3 Global 0.05Deg CMG V006 \[Data set\], https://doi.org/10.5067/MODIS/MOD11C1.006, 2015.](https://doi.org/10.5067/MODIS/MOD11C1.006)
- 1461 Wang, K., Ma, Q., Wang, X., and Wild, M.: Urban impacts on mean and trend of surface incident
1462 solar radiation, *Geophysical Research Letters*, 41, 4664–4668,
1463 <https://doi.org/10.1002/2014GL060201>, 2014.
- 1464 Wang, L., Liu, H., Chen, D., Zhang, P., Leavitt, S., Liu, Y., Fang, C., Sun, C., Cai, Q., Gui, Z., Liang,
1465 B., Shi, L., Liu, F., Zheng, Y., and Griefinger, J.: The 1820s Marks a Shift to Hotter-Drier Summers
1466 in Western Europe Since 1360, *Geophysical Research Letters*, 49, e2022GL099692,
1467 <https://doi.org/10.1029/2022GL099692>, 2022.
- 1468 Wang, R., Gentine, P., Yin, J., Chen, L., Chen, J., and Li, L.: Long-term relative decline in
1469 evapotranspiration with increasing runoff on fractional land surfaces, *Hydrology and Earth System*
1470 *Sciences*, 25, 3805–3818, <https://doi.org/10.5194/hess-25-3805-2021>, 2021a.
- 1471 Wang, Y., Zhao, X., Mamtimin, A., Sayit, H., Abulizi, S., Maturdi, A., Yang, F., Huo, W., Zhou, C.,
1472 Yang, X., and Liu, X.: Evaluation of Reanalysis Datasets for Solar Radiation with In Situ
1473 Observations at a Location over the Gobi Region of Xinjiang, China, *Remote Sensing*, 13, 4191,
1474 <https://doi.org/10.3390/rs13214191>, 2021b.
- 1475 White, M. A., Thornton, P. E., Running, S. W., and Nemani, R. R.: Parameterization and Sensitivity

1476 Analysis of the BIOME–BGC Terrestrial Ecosystem Model: Net Primary Production Controls, Earth
1477 Interactions, 4, 1–85, [https://doi.org/10.1175/1087-3562\(2000\)004<0003:PASAOT>2.0.CO;2](https://doi.org/10.1175/1087-3562(2000)004<0003:PASAOT>2.0.CO;2),
1478 2000.

1479 Yang, D., Chen, H., and Lei, H.: Analysis of the Diurnal Pattern of Evaporative Fraction and Its
1480 Controlling Factors over Croplands in the Northern China, Journal of Integrative Agriculture, 12,
1481 1316–1329, [https://doi.org/10.1016/S2095-3119\(13\)60540-7](https://doi.org/10.1016/S2095-3119(13)60540-7), 2013.

1482 Yang, R. and Friedl, M. A.: Modeling the effects of three-dimensional vegetation structure on surface
1483 radiation and energy balance in boreal forests, Journal of Geophysical Research: Atmospheres, 108,
1484 <https://doi.org/10.1029/2002JD003109>, 2003.

1485 Zhang, C., Long, D., Zhang, Y., Anderson, M. C., Kustas, W. P., and Yang, Y.: A decadal (2008–
1486 2017) daily evapotranspiration data set of 1 km spatial resolution and spatial completeness across
1487 the North China Plain using TSEB and data fusion, Remote Sensing of Environment, 262, 112519,
1488 <https://doi.org/10.1016/j.rse.2021.112519>, 2021.

1489 Zhang, K., Kimball, J. S., Mu, Q., Jones, L. A., Goetz, S. J., and Running, S. W.: Satellite based
1490 analysis of northern ET trends and associated changes in the regional water balance from 1983 to
1491 2005, Journal of Hydrology, 379, 92–110, <https://doi.org/10.1016/j.jhydrol.2009.09.047>, 2009.

1492 Zhang, K., Kimball, J. S., Nemani, R. R., and Running, S. W.: A continuous satellite-derived global
1493 record of land surface evapotranspiration from 1983 to 2006, Water Resources Research, 46,
1494 <https://doi.org/10.1029/2009WR008800>, 2010.

1495 Zhang, K., Kimball, J. S., Nemani, R. R., Running, S. W., Hong, Y., Gourley, J. J., and Yu, Z.:
1496 Vegetation Greening and Climate Change Promote Multidecadal Rises of Global Land
1497 Evapotranspiration, Sci Rep, 5, 15956, <https://doi.org/10.1038/srep15956>, 2015.

1498 ~~Zhang, L., Yu, X., Zhou, T., Zhang, W., Hu, S., and Clark, R.: Understanding and Attribution of~~
1499 ~~Extreme Heat and Drought Events in 2022: Current Situation and Future Challenges, Adv. Atmos-~~
1500 ~~Sci., 40, 1941–1951, <https://doi.org/10.1007/s00376-023-3171-x>, 2023a.~~

1501 ~~Zhang, X., Huang, A., Dai, Y., Li, W., Gu, C., Yuan, H., Wei, N., Zhang, Y., Qiu, B., and Cai, S.:~~
1502 ~~Influences of 3D Sub-Grid Terrain Radiative Effect on the Performance of CoLM Over Heihe River~~
1503 ~~Basin, Tibetan Plateau, Journal of Advances in Modeling Earth Systems, 14, e2021MS002654,~~
1504 ~~<https://doi.org/10.1029/2021MS002654>, 2022.~~

1505 Zhang, Y.: PML V2 global evapotranspiration and gross primary production (2002.07-2019.08),
1506 <https://doi.org/10.11888/Geogra.tpd.270251>, 2022.

1507 Zhang, Y., Kong, D., Gan, R., Chiew, F. H. S., McVicar, T. R., Zhang, Q., and Yang, Y.: Coupled
1508 estimation of 500 m and 8-day resolution global evapotranspiration and gross primary production in
1509 2002–2017, Remote Sensing of Environment, 222, 165–182,
1510 <https://doi.org/10.1016/j.rse.2018.12.031>, 2019.

1511 Zhang, Y., Li, C., Chiew, F. H. S., Post, D. A., Zhang, X., Ma, N., Tian, J., Kong, D., Leung, L. R.,
1512 Yu, Q., Shi, J., and Liu, C.: Southern Hemisphere dominates recent decline in global water
1513 availability, Science, 382, 579–584, <https://doi.org/10.1126/science.adh0716>, [2023b](https://doi.org/10.1126/science.adh0716)2023.

1514 ~~Zhao, B., Zhang, B., Shi, C., Liu, J., and Jiang, L.: Comparison of the Global Energy Cycle between~~
1515 ~~Chinese Reanalysis Interim and ECMWF Reanalysis, J Meteorol Res, 33, 563–575,~~
1516 ~~<https://doi.org/10.1007/s13351-019-8129-7>, 2019.~~

1517